American Mineralogist, Volume 64, pages 469–500, 1979

Magmas and volatile components[1]

PETER J. WYLLIE

Department of Geophysical Sciences, University of Chicago
Chicago, Illinois 60637

Abstract

The trivial quantities of CO_2 and H_2O (or reduced combination of C–H–O–S) in the upper mantle have little effect on the abundant basalts, but H_2O influences magmas generated in peridotite overlying subducted, hydrated oceanic crust, and CO_2 causes the generation of alkalic subsilicic magmas from peridotite beneath continental shields. *PT* sections through the (partly schematic) phase diagram for peridotite–CO_2–H_2O with low (CO_2 + H_2O) and selected CO_2/H_2O, compared with isotherms, illustrate the petrological structure of the upper mantle for different tectonic environments. If vapor is present, the cooler the geotherm, the higher is H_2O/CO_2: only in regions of upwelling can CO_2-rich vapor exist. The solidus surface for peridotite–CO_2–H_2O (P, T, X^V) has been mapped with tentative boundaries marking changes in normative compositions of near-solidus magmas. The restricted area for quartz-normative magmas suggests that if these are to be generated from mantle in subduction zones, there must be active asthenospheric convection carrying hot mantle to shallow levels above dehydration fronts in subducted oceanic crust. Changes in the relative positions of dehydration fronts and solidus boundaries for warm and cool subduction models are illustrated in new diagrams, unencumbered by the need for precise temperatures and depths. Tests for processes require knowledge of the phase relationships in the system basalt–andesite–dacite–rhyolite–H_2O from magma sources at depth to the surface. Data from scattered sources have been synthesized in a $PTX(SiO_2)X(H_2O)$ framework to 35 kbar, and illustrated in sections and projections, including liquidus surfaces for the rock series to 35 kbar, dry, with 5 percent H_2O, and with excess H_2O (saturated). The volatile components become prominent in residual magmas: pegmatites from granitic magmas are enriched in H_2O, and carbonatites from alkalic magmas are extraordinarily enriched in CO_2. The behavior of another volatile component is illustrated by experimental data in $NaAlSi_3O_8$–H_2O–HF at 2.75 kbar. The vapor-saturated liquidus field boundary extends from 808°C–8.5 percent H_2O to 777°C–(9.2 percent H_2O + 1.0 percent HF), and three-phase boundaries demonstrate strong partition of HF into liquid compared with vapor. Details remain uncertain for the sources of volatile components, in mantle reservoirs or recycled through subduction, and of oxygen fugacity and temperature variation with depth in different tectonic environments.

Introduction

Twenty-two years ago, I was sent by the late Professor H. I. Drever of the University of St. Andrews to learn something about the influence of volatile components from Professor O. F. Tuttle, who was then opening up the new field of hydrothermal experimentation at high pressures, along with his colleagues at The Pennsylvania State University and the Geophysical Laboratory. I have been playing with volatile components in silicate and carbonate melts ever since then, and a survey of "Magmas and Volatile Components" is an obvious subject for my Presidential Address. Unfortunately, the subject is now so large that it merits a book. Fortunately, I do not have to write a book, because I have the presidential privilege of selectivity. I have selected a few major topics, and I have tried to set them within a continuous story. The story line suffers from boudinage, but by borrowing from the literature in a few places I have avoided complete separation of my selected topics.

I offer new representations of phase diagrams for

[1] Presidential Address, Mineralogical Society of America. Delivered at the 59th Annual Meeting of the Society, October 24, 1978.

0003-004X/79/0506-0469$02.00

peridotite–CO_2–H_2O and basalt–andesite–rhyolite–H_2O, a new look at the petrological structure of subduction zones, and old but unpublished data on $NaAlSi_3O_8$–H_2O–HF, in the context of the following story. There is evidence that H_2O and CO_2 (or some other organization of C–H–O) are the most abundant volatile components in the mantle. At mid-oceanic ridges, the petrogenesis of the basalts that generate the oceanic crust is barely affected by the trivial amounts of dissolved CO_2 and H_2O, but H_2O is influential in modifying the compositions of magmas generated from peridotite in subduction zones, and CO_2 is influential in the generation of kimberlites and other subsilicic magmas beneath continental shields. Reaction of the oceanic basalt with ocean water causes extensive hydration, and at compressive boundaries dehydration of the subducted slab releases H_2O for the generation of magmas in the subducted crust and overlying peridotite. Eruption of calc-alkaline lavas and emplacement of batholiths is accompanied by the partial fusion of continental crust. In the generation of migmatites and granitic magmas, H_2O is the dominant volatile component. It is in the late stages of fractional crystallization, the closing stages of crystallization of large magma bodies, and in residual magmas that the influence of more exotic volatile components becomes evident. The experimental data on HF are presented as an introduction to these other "mineralizers" and fugitive components. This is followed by brief reference to pegmatites and carbonatites, two residual magmas in which H_2O and CO_2, respectively, become highly concentrated compared with the trace amounts present in mantle peridotite, the ultimate source rock.

Volatile components

Volcanoes provide dramatic evidence for the emergence of volatile components from the earth's interior. The compositions of volcanic gases have been measured, but it is not always clear to what extent these gases are derived from primordial material, or through recycling of the hydrosphere *via* ground water or subduction.

Anderson (1975) presented a very detailed review of some basaltic and andesitic gases, including gases from volcanoes, from hot springs, and from mineral inclusions. The major components of volcanic gases are H_2O, CO_2, SO_2, and H_2, commonly in that order. This is very different from the inferred composition of the magmatic gas of Kilauea at 1,200°C at a pressure of 500 bars, corresponding to sea-floor pressure: 60 percent SO_2, 20 percent H_2O, 10 percent H_2S, and 10 percent CO_2.

Analyses of the glassy selvages of pillows from submarine basalts at depths greater than 500 m suggest that tholeiitic basalts contain approximately 0.2–0.5 weight percent H_2O, whereas deep-sea alkalic basalts contain 0.9–1 percent H_2O (*e.g.* Moore, 1965). The analyses reveal 0–0.02 percent CO_2. Moore *et al.* (1977) determined that mid-ocean-ridge basalts from eruption depths of 2.7 to 4.8 km were saturated with CO_2, and that the vesicles in the glassy selvages contained more than 95 percent CO_2, amounting to 400–900 ppm of the whole rock. They estimated that the magmas had contained 0.08–0.16 percent CO_2 of deep-seated origin.

Results obtained recently by Delaney *et al.* (1978) indicate that H_2O contents of the glassy selvages of submarine basalts may represent contamination by ocean water. They measured the compositions of gases dissolved in glass inclusions trapped in olivine phenocrysts of ocean-ridge basalts. H_2O was virtually absent, and the average CO_2 content was 0.2 percent, somewhat higher than that of the matrix glass.

Anderson's (1975) analyses of glass trapped in large crystals in pumice indicate that 3–5 percent H_2O is commonly dissolved in basaltic and andesite magmas below volcanoes of continental margins associated with compressive plate boundaries.

The evidence that CO_2 is transported from the mantle by magmas and rocks was reviewed by Wyllie (1977a) and Eggler (1978). The existence of diamonds and graphite in peridotite nodules demonstrates that the oxygen fugacity is not high enough to oxidize all carbon at depth. Perchuk (1977) concluded that gases from the mantle are very reduced, including hydrogen and methane. At some level, the components C–H–O are oxidized so that H_2O and CO_2 become dominant. According to M. Sato (personal communication, 1977), there is probably a depth interval within which carbon and carbonate can coexist in the mantle, a view shared by Rosenhauer *et al.* (1977) and Woermann *et al.* (1977). As a first step for interpretation of processes occurring in the system peridotite–C–H–O, I therefore evaluate the phase relationships in the oxidized system, peridotite–CO_2–H_2O.

Melting of mantle peridotite

Although it is established that the mantle is heterogeneous, there is general agreement that most of the upper mantle is composed of a peridotite with major mineralogy olivine and two pyroxenes, together with an aluminous mineral which changes from plagioclase to spinel to garnet with increasing pressure, as shown in Figure 1. Figure 1 is a schematic phase diagram for an "average" peridotite of unspecified

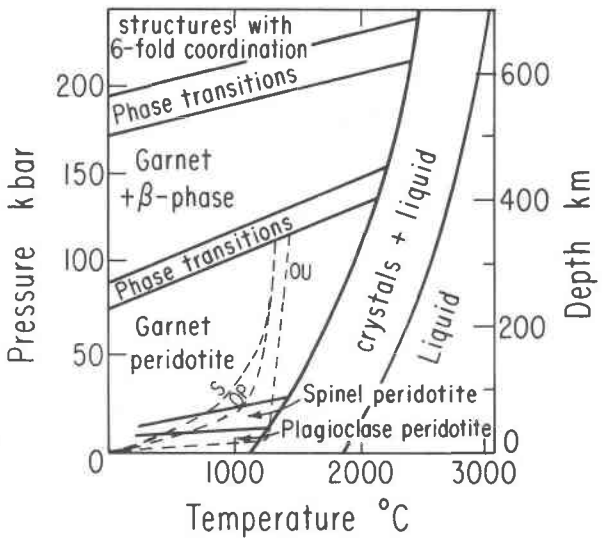

Fig. 1. Schematic phase diagram for peridotite based on data from various sources (Wyllie, 1971, Chapter 6; Wyllie, 1973, Fig. 2; Ringwood, 1975, Chapters 5 and 6; Yoder, 1976, Chapter 2). The dashed lines are geotherms from Solomon (1976). Abbreviations: S = shield; OP = ocean plate; OU = oceanic upwelling, as beneath ocean ridge.

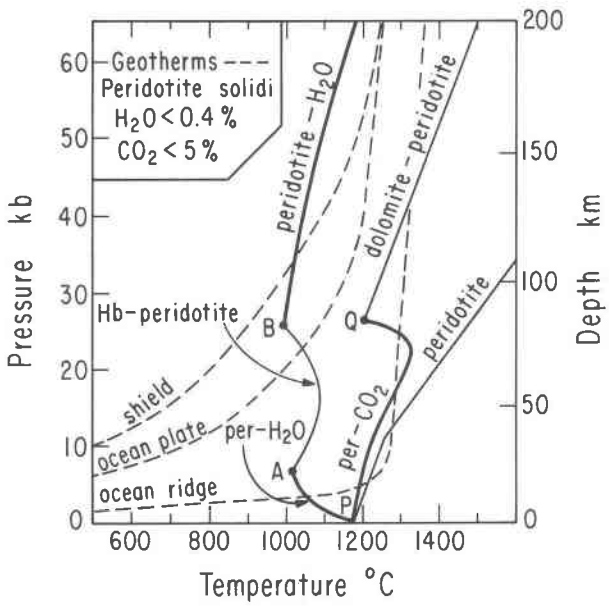

Fig. 2. Comparison of solidus curves for peridotite, for peridotite with CO_2, and for peridotite with H_2O, in part schematic. For sources and the variety of results available see Wyllie (1977a, Fig. 6 and 7A; 1978, Fig. 1 and 2B). The heavy lines show where free vapor exists at the solidus. The dashed lines are geotherms from Fig. 1.

composition, based on data from many sources, with much extrapolation to higher pressures. Partial melting occurs if the temperature exceeds the solidus.

A knowledge of the temperature distribution within the earth as a function of place and time is fundamental for understanding of magmatic processes, but it is not well established. Figure 1 shows three geotherms for convecting mantle according to Solomon (1976). Temperatures in a region of upwelling, beneath ocean ridges for example, are higher than temperatures beneath normal ocean plates. The temperatures shown beneath shield and ocean plates become identical at 200 km depth (contrast Jordan, 1975). The geotherms drawn for lithosphere (shallower than about 100 km) are passed through the zones plotted by Solomon for values estimated from the study of peridotite nodules. The lithosphere geotherms are similar to those calculated for conduction models (*e.g.* Clark and Ringwood, 1964).

According to Figure 1, mantle peridotite rising beneath an ocean ridge does not begin to melt until it reaches a level of about 50 km. Significantly higher temperatures must be achieved to initiate magma generation at depths greater than 100 km.

Effect of H_2O and CO_2

The shallower parts of the three geotherms and the peridotite solidus from Figure 1 are reproduced in Figure 2, and compared with solidus curves estimated for peridotite in the presence of a small amount of H_2O, or of CO_2 (Wyllie, 1977a, 1978). Amphibole is generated in peridotite by reaction with H_2O, between the limits A and B. Up to 0.4 percent H_2O can be stored in amphibole–peridotite. For peridotite with more than 0.4 percent H_2O, the peridotite–H_2O solidus would extend continuously between A and B, as shown in Figure 3A. At shallow depths, the peridotite–CO_2 solidus is not much lower in temperature than the peridotite solidus. The curve is depressed abruptly to the point Q, where dolomite is produced by a carbonation reaction. Dolomite–peridotite can absorb about 5 percent CO_2 without losing one or more of the peridotite minerals; only then does free CO_2 remain. The solidus curve for peridotite with excess CO_2 (Fig. 3A) extends from Q at a temperature somewhat lower than the dolomite–peridotite solidus in Figure 2.

According to Figure 2, the presence of small amounts of H_2O in the upper mantle would produce traces of magma in all tectonic environments at various depths; the presence of small amounts of CO_2 would produce dolomite within and beneath shield and ocean plates (note position of the carbonation reaction in Fig. 4), and traces of magma where upwelling dolomite–peridotite reaches a level of about

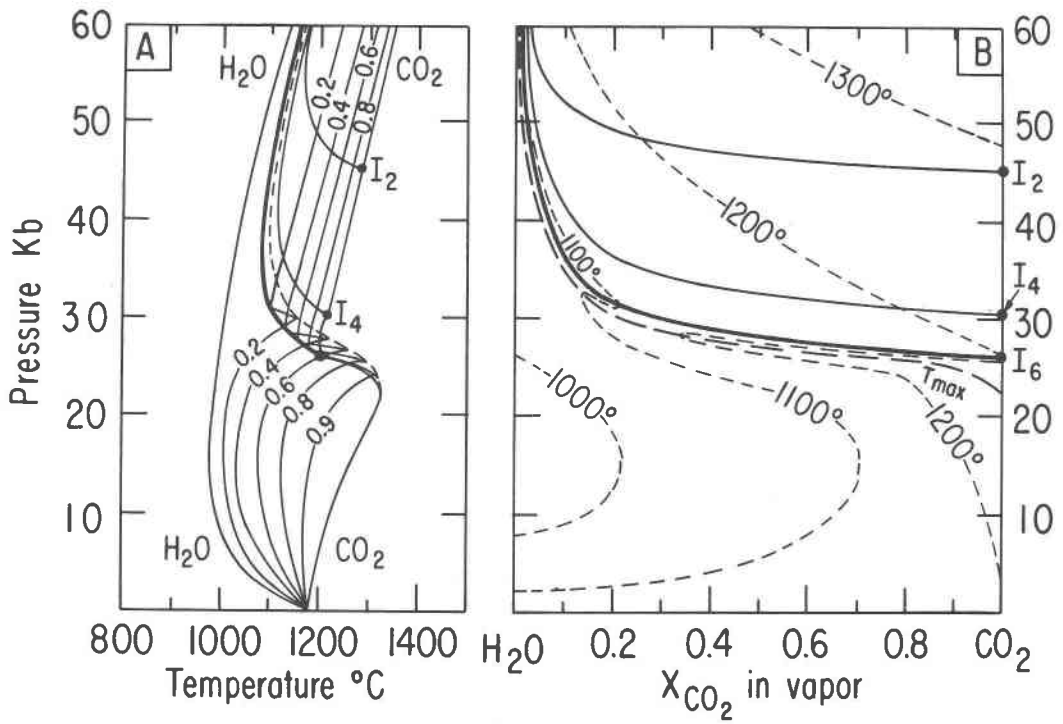

Fig. 3. The shape of the solidus surface for peridotite–CO_2–H_2O illustrated by (A) contours for constant vapor phase composition (molar fractions), and (B) by isotherms (schematic, from Wyllie, 1978, Fig. 4). Note the thermal ridge on the solidus marked by the dashed line (Tmax in Fig. B). The heavy lines extending from I_6, I_4, and I_2 are vapor-buffer lines corresponding to the three carbonation reactions, (6), (4), and (2), respectively. For details see text and Wyllie (1977a, 1978).

140 km. The conditions for melting between these limiting conditions are more complex, involving peridotite minerals, hydrous minerals, carbonates, and vapors variable between CO_2–H_2O.

The system peridotite–CO_2–H_2O

Experimental studies on the effect of CO_2–H_2O mixtures on the melting of natural peridotites (Mysen and Boettcher, 1975), and of synthetic forsterite + enstatite (Eggler, 1975), established the near-solidus phase relationships for peridotite–CO_2–H_2O up to 20 kbar. Subsolidus carbonation reactions involving peridotite minerals, discovered by Wyllie and Huang (1975, 1976) and Eggler (1976), produce striking changes in the melting relationships between about 20 and 30 kbar. Ellis and Wyllie (1979a, 1979b, 1979c) extended theoretical calculations to 100 kbar in the model system MgO–SiO_2–CO_2–H_2O in order to examine the effects of carbonation, hydration, and CO_2–H_2O mixtures on the melting of forsterite + enstatite. Eggler (1977, 1978) and Wyllie (1977a, 1978) combined available experimental data from natural rocks with phase equilibrium data from synthetic systems to analyze the phase relationships in the system peridotite–CO_2–H_2O.

Phase relationships

Figures 3, 4, and 5 illustrate the phase relationships with excess vapor. These are not experimentally-determined diagrams, although they are constructed around experimental data. Unfortunately, for those parts of the system that have been investigated experimentally there are different results from different laboratories and for different peridotites. The phase relationships are illustrated in terms of pressure and temperature, and a third axis for variable vapor phase composition between CO_2–H_2O (mole fraction). The figures are based on the values adopted by Wyllie (1977a, 1978). Precise values are plotted against the P, T, and X axes to maintain consistency among the figures. This may give a semblance of accuracy, which I do not claim. Precise values for many parts of the phase diagrams need experimental determination, but I believe that the topology of the phase diagrams, the general geometrical relationships, will not be significantly changed by these determinations. The diagrams serve as guides for additional experimental studies, as well as for interpretation of the melting relationships in the system.

Figure 3 defines the shape of the solidus surface. In

the *PT* projection (Fig. 3A), the contours for vapor phase composition illustrate the general decrease in solidus temperature from CO_2 to H_2O (compare Fig. 2); this is also illustrated by the isotherms in the *PX* projection (Fig. 3B).

The solidus surface is traversed by three univariant lines, extending from invariant points I_6, I_4, and I_2 in the system peridotite–CO_2, which define the intersections between the solidus surface and three subsolidus divariant carbonation reactions (Wyllie, 1977a; 1978, Fig. 3). The reactions in the direction of increasing pressure, as identified in the model system $CaO–MgO–SiO_2–CO_2$ by Wyllie and Huang (1975, 1976), are:

$$\text{olivine} + \text{clinopyroxene} + CO_2 = \text{orthopyroxene} + \text{dolomite}_{ss} \quad (6)$$

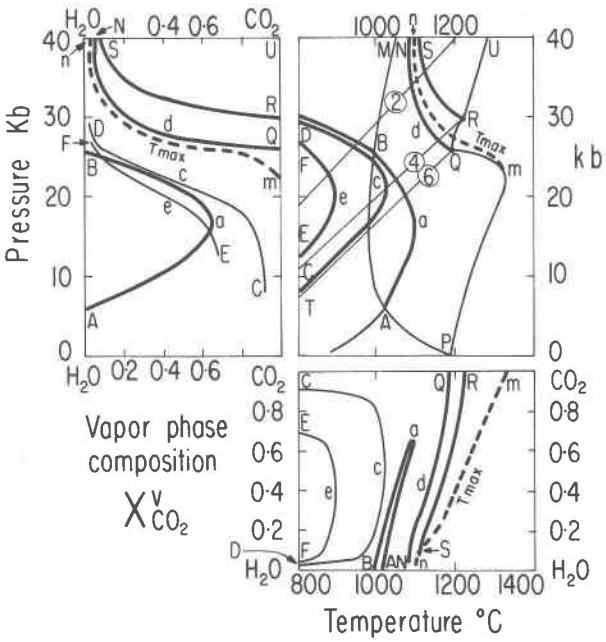

Fig. 4. The system peridotite–CO_2–H_2O with excess vapor, showing phase relationships on the solidus surface, subsolidus reactions involving hydration to produce amphibole and carbonation to produce dolomite and magnesite solid solutions, and subsolidus reactions between the hydration and carbonation reactions (largely schematic). It is assumed that there is insufficient K_2O for phlogopite to grow. This is based on the diagrams constructed by Wyllie (1978, Figs. 7A and 9A), with some additional features. In the *PT* projection, light lines refer to reactions with either CO_2 or H_2O, and heavy lines refer to reactions with mixed H_2O–CO_2 vapor. The *PX* and *TX* projections (molar fractions) give the compositions of vapors as a function of *P* and *T*; the light lines refer to subsolidus reactions, and the heavy lines refer to the divariant buffer reactions on the solidus surface. Compare Fig. 3 (Q = I_6, R = I_4).

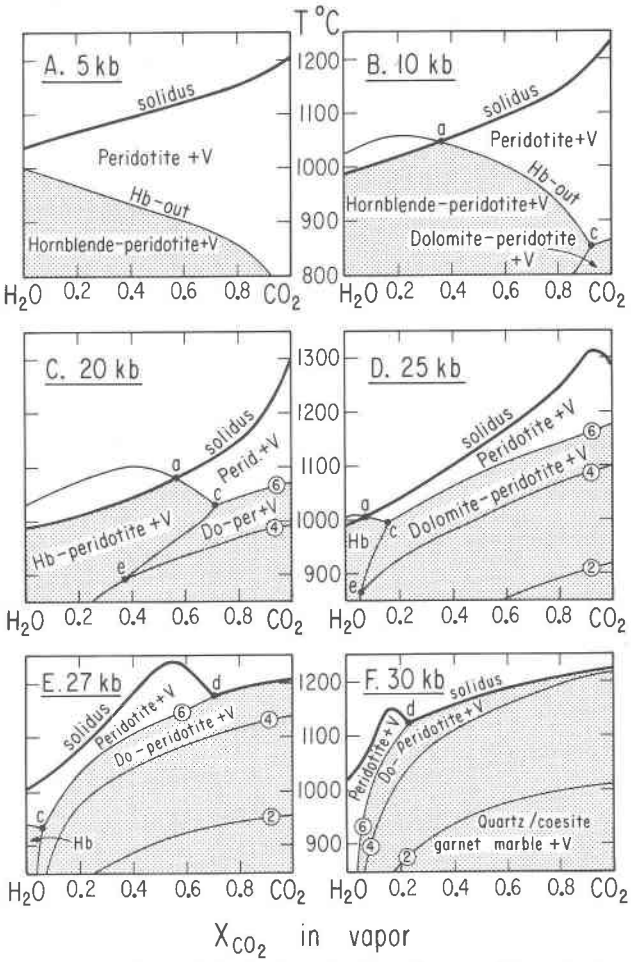

Fig. 5. Schematic isobaric projections from peridotite–CO_2–H_2O with excess vapor (omitting phlogopite) modified and extended from Wyllie (1978, Figs. 6 and 10). The isobaric invariant points a, d, c, and e are from univariant lines in Fig. 4. Carbonation reactions (6), (4), and (2) are identified in the text. The conditions in the shaded areas cannot be achieved for peridotite with less than 0.4 percent H_2O and 5 percent CO_2.

$$\text{olivine} + \text{dolomite}_{ss} + CO_2 = \text{orthopyroxene} + \text{magnesite}_{ss} \quad (4)$$

$$\text{orthopyroxene} + \text{dolomite}_{ss} + CO_2 = \text{quartz/coesite} + \text{magnesite}_{ss} \quad (2)$$

It requires about 5 percent CO_2 to react away all of the clinopyroxene in peridotite (6), and about 23 percent to transform peridotite completely into coesite–garnet marble *via* the three reactions.

The dashed line in Figure 3A corresponds to the long-dashed line labelled *T*max in Figure 3B. The line *T*max is the crest of a thermal ridge on the solidus surface, as shown by the two sets of contours in Figure 3. It is identified as mn in Figure 4.

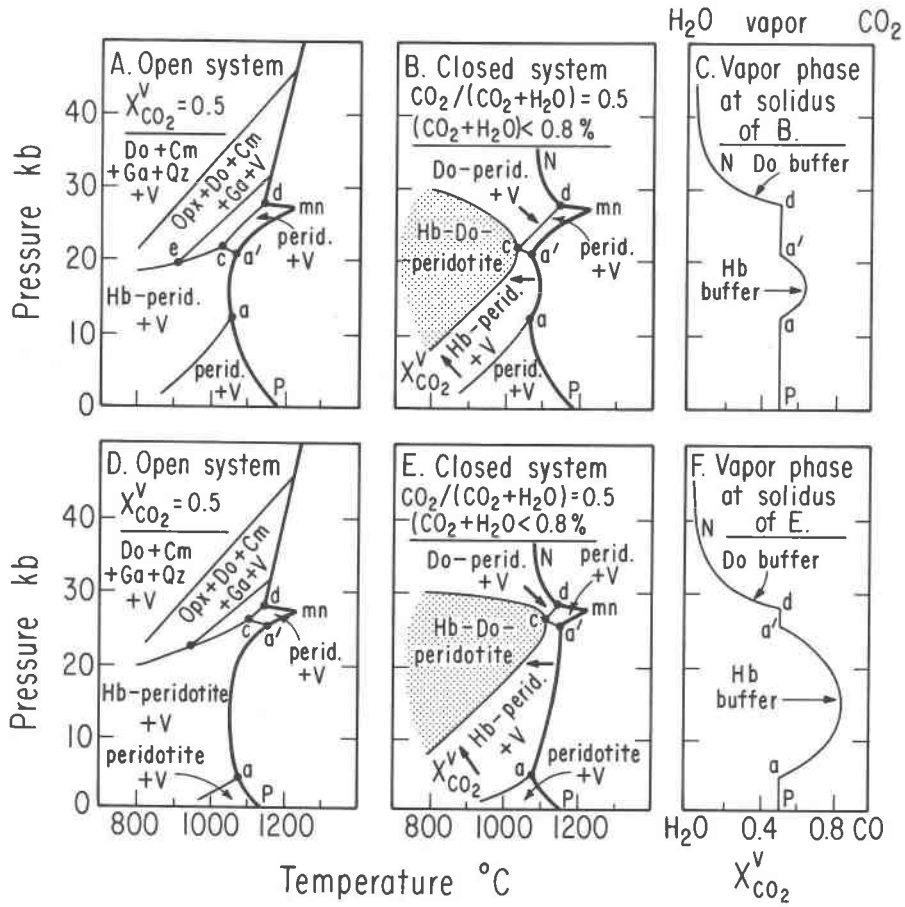

Fig. 6. Schematic phase relationships in the system peridotite–CO_2–H_2O using two different experimental results for amphibole. A, B, and C after Millhollen *et al.* (1974); D, E, and F after Green (1973a). The heavy arrows show the directions of increasing $X^V(CO_2)$ on divariant vapor-buffered reaction surfaces. Points a, c, and d are located on univariant curves in Fig. 4. Abbreviations: Hb–amphibole, Do–dolomite, Opx–orthopyroxene, Ga–garnet, Cm–magnesite solid solution, Qz–SiO_2 polymorphs.

Figure 4 shows two of the univariant curves of Figure 3 (Q = I_6, R = I_4) in *TX* as well as *PT* and *PX* projections, in addition to the univariant curve AaB on the solidus surface. The line AaB marks the intersection of the subsolidus divariant dehydration surface for amphibole in the presence of H_2O–CO_2 mixtures (Wyllie, 1978, Fig. 7A). The carbonation surface for reaction (6) with H_2O–CO_2 intersects the amphibole dehydration surface along the univariant line CcD (Wyllie, 1978, Fig. 9A). Similarly, the surface CcDFeE for amphibole–dolomite–peridotite with excess vapor intersects the carbonation surface for reaction (4) with H_2O–CO_2 along the univariant line EeF (estimated). The geometry of these lines, and the divariant surfaces connecting them, can be visualized in sections through the *PTX* model (Figs. 5 and 6).

The isobaric sections in Figure 5 show the changing curvature of the solidus with increasing pressure, the appearance of the temperature maximum in Figure 5D (at pressure between m and Q in Fig. 4), the intersection of carbonation reaction (6) with the solidus at point d in Figures 5E and F (see QdN in Fig. 4), and the enrichment of vapor d in H_2O/CO_2 through a small pressure increase.

The geometry of the amphibole dehydration surface and its intersections with other surfaces can be traced in Figures 4 and 5. The amphibole surface intersects the solidus along the line AaB (Fig. 4, points a in Fig. 5), and the carbonation reaction (6) along the line CcD (Fig. 4, points c in Fig. 5). At temperatures below c, the amphibole field is bounded by a divariant exchange reaction from amphibole– to dolomite–peridotite (assumed, estimated, not determined), which intersects the carbonation reaction (4) along the line EeF (Fig. 4, points e in Fig. 5).

Figures 5B and C are modified from Wyllie (1978, Fig. 10), where I assumed for simplicity that the

temperature maximum for amphibole dehydration coincided with the solidus intersection, at points a, following model systems of Eggler (1973, Fig. 44, 8.4 kbar; 1978, Fig. 19, $P = 6$). The alternative model arrangement, shown in Figure 5, is adopted here because Allen and Boettcher (1978) have established experimentally the existence of similar temperature maxima for amphibole in the systems basalt–H_2O–CO_2 and andesite–H_2O–CO_2. The projected temperature maximum for amphibole (in the presence of liquid and vapor), which would plot as a line AB at somewhat higher temperature than AaB in Figure 4, coincides with the vapor-absent solidus for amphibole–peridotite drawn as AB in Figure 2.

Buffering of vapor and liquid compositions by amphibole and dolomite

The univariant lines projected in Figure 4 and the divariant surfaces intersected in Figure 5 are for reactions occurring in the presence of vapor, which requires that there is sufficient $H_2O + CO_2$ present to permit completion of the subsolidus hydration and carbonation reactions, and to saturate the liquids. A minimum of 0.4 percent H_2O is required to complete the formation of amphibole–peridotite, and 5 percent CO_2 is required to complete reaction (6) and replace all clinopyroxene in peridotite with dolomite.

For peridotite with less than 0.4 percent H_2O and 5 percent CO_2, the conditions in the shaded areas of Figure 5 cannot be achieved. The vapor phase compositions are limited to the areas labelled peridotite + V. If either amphibole or dolomite is produced, the vapor phase composition is then buffered to remain on the corresponding reaction surface. If both amphibole and dolomite are produced, the vapor phase is even more closely buffered to the points c (line CcD in Fig. 4); with slight decrease in temperature, all vapor must react producing vapor-absent amphibole–dolomite–peridotite. Amphibole–dolomite–peridotite with vapor buffered along the lines ce (Figs. 5C and D) can exist only if the system contains either more than 0.4 percent H_2O, or more than 5 percent CO_2.

Consider the effect of heating amphibole–peridotite that coexists with CO_2–H_2O vapor (less than 0.4 percent H_2O). In Figure 5B, amphibole dissociates, and the vapor follows a path along ca to the solidus at a, where both vapor phase and coexisting liquid compositions are fixed. Alternatively, if all amphibole dissociates before melting begins, peridotite–vapor will melt at the point on the solidus corresponding to CO_2/H_2O in the system. In terms of Figure 4, the amphibole–peridotite either begins to melt with buffered vapor along the line AaB (and correspondingly fixed liquid compositions), or at some point on the divariant solidus surface, AaBPQ.

Similarly, dolomite–peridotite coexisting with vapor (with less than 5 percent CO_2) is constrained to remain on the surface for reaction (6), and buffered melting begins at points d in Figure 5 (or along the line QdN in Fig. 4). As illustrated by the line QdN in Figure 4, the buffered vapor at the solidus for dolomite–peridotite is greatly enriched in H_2O within a narrow pressure interval above the point Q for pure CO_2. At pressures above 30 kbar, the vapor phase in peridotite–CO_2–H_2O with less than 5 percent CO_2 is forced to high values of H_2O/CO_2 (Fig. 5F). The divariant surface for melting of peridotite–vapor is correspondingly limited.

Figure 6A is a slice through the *PTX* model for the system peridotite–CO_2–H_2O with excess vapor of fixed composition, corresponding to an open system. As reactions proceed, H_2O or CO_2 is added to or subtracted from the system in order to maintain constant vapor composition. Each phase boundary corresponds to a contour on a divariant surface. The temperature maximum on the solidus surface shown in Figures 3, 4 (mn), 5D, 5E, and 5F is clearly displayed in Figure 6A by the point mn on the peridotite + vapor solidus, a'd. With sufficient CO_2 available (about 23 percent), peridotite is converted to garnet–coesite–marble by completion of reaction (2), as depicted also in Figure 5F.

In Figure 6B, representing a closed system with less than 0.4 percent H_2O, the vapor phase in the areas peridotite + V is the same as the vapor in Figure 6A. With formation of amphibole, however, the vapor phase is buffered to remain on the amphibole dehydration surface, and the composition trend of the variable vapor is shown by the heavy arrows for increasing CO_2/H_2O. Similarly, with the formation of dolomite (less than 0.4 percent CO_2 in this example), the vapor phase is buffered to remain on the carbonation surface (6), with vapor-phase composition changing as shown by the heavy arrow. These two surfaces meet at point c (compare Fig. 5) on the amphibole–dolomite buffer line CcD (see Fig. 4). At lower temperatures, all CO_2 and H_2O is stored in vapor-absent amphibole–dolomite–peridotite. Under these conditions, the mineralogy of the subsolidus peridotite is modified only by addition of phases and not by the loss of any of the original peridotite minerals.

Figure 6C shows the vapor-phase composition at

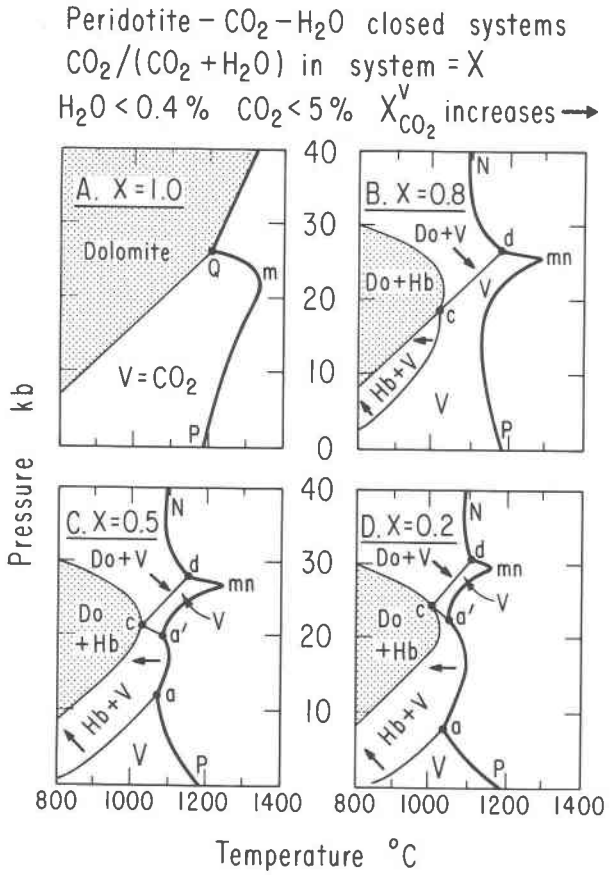

Fig. 7. Phase fields intersected by peridotite–CO_2–H_2O as a function of (H_2O + CO_2) and CO_2/H_2O. Heavy arrows show the directions of increasing $X^V(CO_2)$ in divariant vapor. Vapor is absent in the shaded areas for the stipulated compositions. Compare Fig. 6B.

the solidus for the closed system of Figure 6B. The vapor phase is fixed corresponding to CO_2/H_2O in the system where peridotite + V melts along Pa and a'd, but the presence of amphibole or dolomite at the solidus buffers the vapor. Melting of amphibole–peridotite begins with vapor along the line aa' in Figure 6C, somewhat enriched in CO_2 in accordance with the solidus buffer AaB in Figure 4. Melting of dolomite–peridotite begins with vapor along the line dN in Figure 6C, greatly enriched in H_2O in accordance with the solidus buffer QdN in Figure 4. The solidus for buffered amphibole–peridotite, aa' in Figure 6B, is higher than that for the vapor-excess solidus, aa' in Figure 6A. The solidus for buffered dolomite–peridotite in Figure 6B, in contrast, is at a lower temperature than the vapor-excess solidus curve above d in Figure 6A.

Figures 6D–F are constructed on the basis of Green's (1973a) experimental data for amphibole in peridotite–H_2O (Wyllie, 1978, Figs. 1, 7B, 8, and 9B). Although the shapes and positions of phase boundaries differ from those in Figures 6A–C, and the larger field for amphibole buffers the vapor along aa' to higher CO_2/H_2O, the basic geometry remains unchanged. All features of the phase diagrams in Figures 6A–C are reproduced in Figures 6D–F.

In summary, the solidus for peridotite–CO_2–H_2O is a divariant surface, traversed by a series of univariant lines where the vapor composition is buffered by reaction to produce carbonates or hydrous minerals. The liquid composition is similarly defined at each point on a vapor-buffer line. For peridotite with sufficient K_2O for the production of phlogopite, there are additional curves on the solidus surface for phlogopite and dolomite–phlogopite buffers (Wyllie, 1978, Figs. 12–16). Depending upon the amounts of CO_2 and H_2O in the system, and on CO_2/H_2O, melting may begin either on the divariant solidus surface, or on one of the buffer lines.

Effect of CO_2/H_2O on phase relationships

Figure 7C reproduces Figure 6B. The other diagrams in Figure 7 show how the geometry of the peridotite phase fields changes as a function of CO_2/H_2O in a closed system with insufficient H_2O and CO_2 for completion of hydration and carbonation (6) reactions. Vapor is absent in the shaded areas, of constant composition in the areas labelled V, and variable (buffered) in areas with heavy arrows showing the direction of increasing $X^V(CO_2)$.

Figure 7A shows the solidus for peridotite–CO_2 from Figure 2, and the carbonation reaction (6) dividing the subsolidus field into vapor-present and vapor-absent areas. Addition of a small proportion of H_2O in Figure 7B introduces amphibole in subsolidus fields, and lowers the solidus curve in two distinct regions. Amphibole is produced in dolomite–peridotite within the buffered reaction boundary CcD (compare Fig. 4), and vapor-buffered fields for amphibole–peridotite and dolomite–peridotite are produced on either side of the field for vapor-absent amphibole–dolomite–peridotite. The high-pressure solidus for dolomite–peridotite is depressed all the way to the line dN, part of the dolomite buffer curve QdN of Figure 4. The low-pressure solidus is lowered to the contour line Pmn (see 0.8 in Fig. 3A). The temperature maximum m in Figure 7A is represented by the point mn in Figure 7B, situated on the dashed line in Figure 3A (the line mn in Fig. 4).

With additional H_2O, the low-pressure solidus migrates to lower temperature (Fig. 3), and the field for

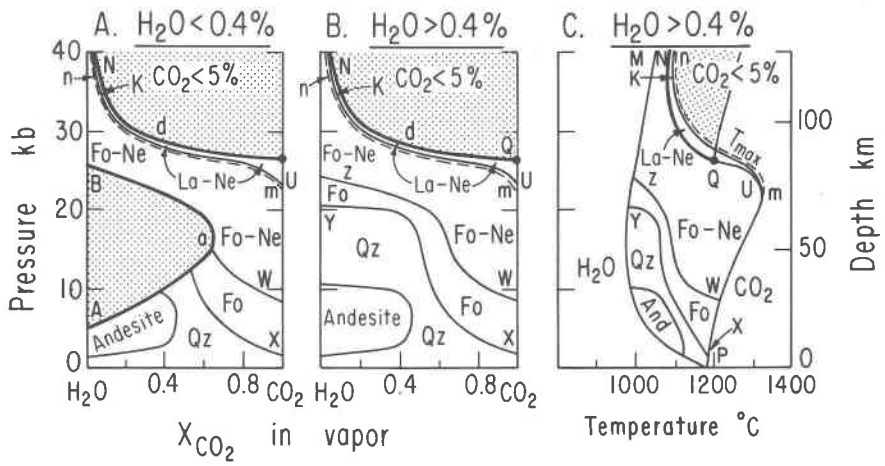

Fig. 8. Projections of the solidus surface for peridotite–CO_2–H_2O (compare Figs. 3 and 4) with tentative boundaries showing the changes in normative composition of the near-solidus, vapor-saturated liquids. Conditions in the shaded areas cannot be achieved for the stipulated conditions. Additional abbreviations: Fo–forsterite, Ne–nepheline, La–larnite. Fo–Ne is forsterite–nepheline-normative liquid.

amphibole–peridotite expands until it crosses the peridotite + V solidus as shown in Figures 7C and D. Buffered amphibole–peridotite then melts along the line aa′, part of the line AaB in Figure 4. Further increase of H_2O/CO_2 causes minor changes in the temperatures of phase boundaries, but no changes in phase fields intersected, as shown in Figure 7D. The diagram for peridotite–H_2O (see Fig. 2) differs from Figure 7D by loss of the temperature maximum mn, of dolomite, and of buffered vapor, and by expansion of the vapor-absent field to the solidus.

Effect of CO_2/H_2O on mantle magma compositions

The solidus surface for peridotite–CO_2–H_2O is shown in *PX* projections in Figures 8A and B, and in *PT* projection in Figure 8C (compare Figs. 3 and 4). With H_2O less than 0.4 percent, no melting can occur in the shaded area enclosed by the amphibole buffer line AaB in Figure 8A. With CO_2 less than 5 percent, no melting can occur in the shaded area above the dolomite buffer line QdN in Figure 8.

Although small percentages of H_2O + CO_2 are completely dissolved by the liquid a few degrees above the solidus at high pressures, the first liquid produced (in the presence of vapor) is saturated with H_2O + CO_2. It was confirmed experimentally by Mysen and Boettcher (1975) for peridotite, and by Eggler (1975) for synthetic systems, that up to at least 20 kbar, H_2O/CO_2 is greater in liquid than in coexisting vapor, a result anticipated from the known solubilities of H_2O and CO_2 in silicate liquids. In synthetic silicate–carbonate–CO_2–H_2O systems, however, H_2O/CO_2 is greater in vapor than in coexisting liquid (Wyllie, 1978; Ellis and Wyllie, 1979c). This fact suggests that the liquids coexisting with vapor along the dolomite–peridotite buffer line QdN are enriched in CO_2 relative to coexisting vapors, a reversal of the distribution of H_2O and CO_2 at lower pressures. Wyllie (1978) proposed that the reversal occurred along the azeotropic maximum on the solidus surface, the dashed line mn, where H_2O/CO_2 in liquid and vapor are equal. The solidus surface is therefore divided into two parts by the line mn. On the H_2O side of the line (the area PmnMP):

$$(H_2O/CO_2)^V < (H_2O/CO_2)^L \qquad \text{(the liquid prefers } H_2O\text{)}$$

On the CO_2 side of the line (the area mmNQ):

$$(H_2O/CO_2)^V > (H_2O/CO_2)^L \qquad \text{(the liquid prefers } CO_2\text{)}$$

There have been several experimental studies and many controversial reviews concerned with the compositions of near-solidus liquids from peridotite in the presence of H_2O at high pressures (*e.g.* Kushiro, 1972; Nicholls, 1974; Nehru and Wyllie, 1975; Mysen and Boettcher, 1975; Green, 1976). The debate focusses on the depth to which andesitic liquids may be produced, and the depth at which the liquid changes from quartz-normative to forsterite-normative.

There have been no experimental studies on the compositions of liquids from peridotite–CO_2, but studies in synthetic model systems demonstrate that the SiO_2 content of near-solidus liquids is decreased by increasing pressure. Low-pressure quartz-normative liquids are assumed to change to forsterite-normative at 1.3 kbar (*X* in Fig. 8), consistent with the change from incongruent to congruent melting of

enstatite reported by Chen and Presnall (1975). Forsterite-normative liquid becomes larnite-normative at some pressure above 20 kbar in the synthetic system (Eggler, 1974), as the liquid migrates towards the lower-temperature silicate–carbonate liquids (Wyllie and Huang, 1975). At Q in Figure 8, the first liquid produced from melting of dolomite–peridotite is so rich in CO_2 that it is at least "kimberlitic" with up to 27 percent CO_2 (Eggler, 1978), and possibly "carbonatitic" with 35–40 percent CO_2 (Wyllie and Huang, 1975; Wyllie, 1977a, 1978).

There are only two relevant experimental studies on the compositions of glasses quenched from liquids with $CO_2 + H_2O$. Eggler (1975) studied forsterite–enstatite at 20 kbar, and Mysen and Boettcher (1975) studied four peridotites from 10 to 20 kbar. These results indicate that near-solidus liquids are quartz-normative for vapors up to about $X^V(CO_2) = 0.5$ between 10 and 20 kbar. In the presence of vapors with greater $X^V(CO_2)$, Mysen and Boettcher reported glasses that were nepheline-normative, and even larnite-normative at 10 and 15 kbar.

The compositions of near-solidus liquids in the system peridotite–CO_2–H_2O have been discussed by Mysen and Boettcher (1975), Eggler (1978), and Wyllie (1978). No consistent scheme emerges from the available data and inferences, but Figure 8B is an attempted compromise which illustrates the major trends. The chemical variation is shown by the lines representing changes in the normative composition of near-solidus liquids.

The line XY marks the fundamental change from quartz-normative to forsterite-normative. The smaller area for andesitic liquids is based on the results of Nicholls (1974) with H_2O, but Mysen and Boettcher (1975) would expand the andesite field upwards in pressure at least to the line YX. Green (1976) argued that the andesitic glasses obtained from 20 kbar runs by Mysen and Boettcher had changed during quenching, compared with the original liquids.

The line ZW for normative nepheline is quite arbitrary. The results of Mysen and Boettcher (1975) suggest that ZW is close to XY between 10 and 20 kbar. Kushiro (1972) and Mysen and Boettcher (1975) would probably prefer to see point Z located at higher pressures.

Wyllie (1978) suggested that the change to larnite-normative liquids (Eggler, 1974) was associated with the change in distribution of H_2O and CO_2 between liquid and vapor, and therefore with the *T*max on the solidus surface. The boundary proposed is UK, located near to the line mn in Figure 8. This is not consistent with the larnite-normative glasses at 10 kbar, reported by Mysen and Boettcher (1975).

The boundaries on Figure 8B have been transferred to the *PT* projection in Figure 8C, using contours from Figure 3A as a guide. The siliceous liquids are restricted to the low-temperature, low-pressure part of the solidus surface (Fig. 8C), as well as to vapors relatively high in H_2O/CO_2 (Fig. 8B). For systems with less than 0.4 percent H_2O, the siliceous liquids are limited to even lower pressures, because the quartz-normative field is cut off by the amphibole buffer, Aa in Figure 8A.

Figure 8 gives the compositions of liquids developed in peridotite with CO_2–H_2O mixtures only at the initial stages of magma generation. The amount of liquid developed at the solidus depends upon the amount of total $H_2O + CO_2$. With increased temperature above the solidus, the temperature interval for the coexistence of vapor with crystals + liquid also depends upon the amount of total $H_2O + CO_2$. At high pressures, there is a wide melting interval between the solidus surface in Figure 8 and the solidus for peridotite without volatile components (see Fig. 2). The paths followed by liquids through this interval introduce prospects for the generation of an even wider range of magma compositions than those mapped on the solidus surface.

Mantle cross-sections and magma generation

Many investigators have considered mantle cross-sections for peridotite with a trace of H_2O (*e.g.* Lambert and Wyllie, 1968; Green and Liebermann, 1976), or with a trace of CO_2 (*e.g.* Eggler, 1976; Wyllie and Huang, 1976; Presnall, 1979). Wyllie (1977a, Fig. 11) constructed cross-sections for peridotite with CO_2–H_2O mixtures, showing the effect of dolomite but neglecting the formation of hydrous minerals such as amphibole and phlogopite. Phase diagrams such as those in Figures 6 and 7 now permit evaluation of the distribution of amphibole, dolomite, and CO_2–H_2O vapor in the upper mantle for any required CO_2/H_2O. Consideration of phlogopite as well introduces even more variability (Wyllie, 1978, Figs. 9, 12, and 16). Eggler (1977) concluded that there is a unique mantle solidus provided that the volatile components are present below the limits given for Figure 7, and with compositions within the range $CO_2/(CO_2 + H_2O) = 0.15$–$0.85$ (molar). The mantle solidus is only "unique" where it corresponds to one of the solidus buffer curves. According to Figure 7, the mantle solidus curve is not made up exclusively of univariant buffers, and its position varies progressively as a function of H_2O/CO_2 in mantle peridotite.

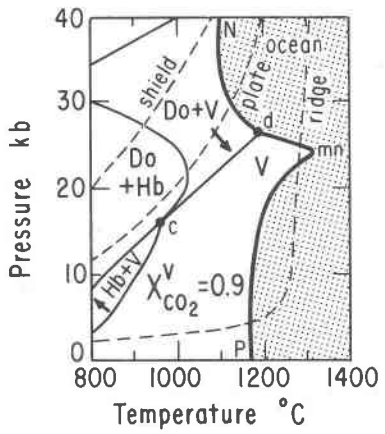

Fig. 9. Phase fields intersected by peridotite–CO_2–H_2O for conditions stipulated in Fig. 7, compared with geotherms from Figs. 1 and 2.

Figure 9 gives the phase relationships for peridotite with a small amount of total volatiles and high CO_2/H_2O (X = 0.9, with conditions as specified for Fig. 7). This corresponds to a section between those in Figures 7A and 7B. Geotherms for three different tectonic environments are reproduced from Figure 2, which compares these geotherms with solidus curves for the limiting cases of peridotite, peridotite–H_2O, and peridotite–CO_2.

Mantle cross-sections

Assuming a mantle composed of peridotite, with 0.1 weight percent CO_2 and $CO_2/(CO_2 + H_2O)$ = 0.9 (molar fraction), the phase assemblages present at each depth are determined by following a geotherm through the phase diagram in Figure 9. Mantle cross-sections derived in this way are given in Figure 10.

Beneath continental shields and stable ocean plates, all CO_2 and H_2O is stored in vapor-absent dolomite–amphibole–peridotite down to the depth where amphibole becomes unstable. (If H_2O > 0.4 percent, dolomite–amphibole–peridotite would coexist with vapor buffered along the boundary CcD in Figs. 4 and 5.) At greater depths, dolomite–peridotite coexists with vapor, and the vapor composition is buffered according to position on the divariant surface for carbonation reaction (6). Vapor-phase compositions are plotted in Figure 10D.

Within the oceanic lithosphere, the vapor phase is significantly enriched in H_2O, despite the high CO_2/H_2O in the system as a whole. $X^V(CO_2)$ decreases from about 0.4 to 0.3 as depth increases from about 75 to 100 km. Within the continental lithosphere, the vapor phase is even richer in H_2O, with $X^V(CO_2)$ about 0.1 between about 85 and 130 km.

Incipient melting begins beneath both continental and stable ocean lithosphere at the depth where the geotherm crosses the dolomite-buffer curve dN (a part of QdN in Figure 4). As shown in Figures 4, 9, and 10D, the initial melting occurs in the presence of vapor enriched in H_2O, but the initial liquid contains a high percentage of CO_2 (because of the presence of subsolidus dolomite), and very low SiO_2. Liquids developed along the line QdN are nepheline–larnite–normative (Fig. 8). With increasing depth, the proportions of interstitial liquid would change only slightly, but the liquid would change progressively towards more siliceous compositions.

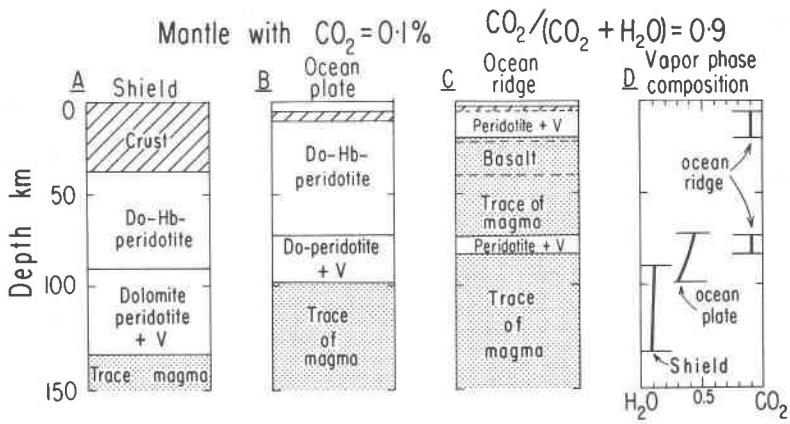

Fig. 10. Cross-sections through mantle with volatile contents as shown, based on the phase diagram and geotherms given in Fig. 9. Note that beneath ocean ridges there are two layers of partial melting, with larger proportions of basaltic magma generated at shallow levels (see Fig. 2). For each layer with vapor in diagrams A, B, C, the vapor composition is shown in diagram D. Dolomite buffers the vapor composition to enrichment in H_2O. It is impossible for CO_2-rich vapor to exist in the mantle beneath the shields (see Figs. 9 and 4); phlogopite can coexist with dolomite.

The cross-sections in Figures 10A and B can be modified for mantle peridotite with sufficient K_2O to permit the growth of phlogopite, using other phase diagrams (Wyllie, 1978, Figs. 12–16). The dolomite–peridotite is then replaced either by phlogopite–dolomite–peridotite with vapor compositions buffered to values very similar to those given in Figure 10D, or by vapor-absent phlogopite–dolomite–peridotite if there is insufficient H_2O present to make the maximum amount of phlogopite appropriate for the bulk composition (Holloway and Eggler, 1976). These alternatives involve minor adjustments in solidus temperatures and depths to the zone of incipient melting, and changes in the compositions of interstitial magmas that are surely significant, but not yet determined.

In a region of upwelling mantle, represented by the ocean-ridge section in Figure 10C, the geotherm does not pass through phase fields including dolomite or amphibole. The vapor, therefore, where present, has the CO_2-rich composition corresponding to CO_2/H_2O of the system (Fig. 10D). The geotherm passes through two regions of incipient melting. The deeper region below about 80 km in Figure 10C is similar to that for the other cross-sections. The shallower interval, extending between about 75 and 20 km, differs in several respects. The distribution of H_2O and CO_2 between liquid and vapor is reversed, with H_2O dissolving preferentially in the liquid, because this part of the solidus is on the H_2O side of the line mn (Fig. 8). The liquid composition is therefore more siliceous than that in the deeper zone. The amount of liquid present is much higher, especially at shallower depths where the geotherm crosses the peridotite solidus (Fig. 2) and produces liquid of normal basaltic composition. In this interval, labelled in Figure 10C as "basalt," the percentages of CO_2 and H_2O dissolved in the interstitial basaltic liquid are very low.

The situation illustrated in Figure 10C is not stable. Associated with the process of mantle upwelling is the removal of magma from the peridotite mush, the formation of magma chambers at high levels in the upper mantle and oceanic crust, and the eruption of lavas from the spreading region. During this process, the rising magmas would tend to retain dissolved H_2O and evolve CO_2, as the CO_2 solubility in magmas decreases to very low levels at low pressures.

Presnall (1979), impressed with the evidence for extremely high values of CO_2/H_2O in oceanic basalts, considered the phase relationships in peridotite–CO_2 and introduced the idea of a "double low-velocity zone" associated with ocean ridges. The intersections of geotherm and peridotite–CO_2 solidus are shown in Figure 2. Similar intersections occur for peridotite with H_2O in addition to CO_2, as shown in Figures 9 and 7. If the low seismic velocities are correlated with the presence of interstitial magma, then Figures 10B and C illustrate a structure that should give a double low-velocity zone beneath the ridges, with the shallower zone becoming pinched out as temperatures decrease with distance from the ridge crest.

Another possibility is introduced for mantle with H_2O/CO_2 high enough to reduce the temperature of solidus point mn below the ridge geotherm (compare Figs. 9 and 7). Under these conditions, the low-velocity zone beneath the ridge would extend all the way to shallow levels, with no intervening subsolidus layer near 75 km. Some distance from the ridge, however, decreasing temperatures would lower the geotherm below the solidus near point mn, and a double low-velocity zone would develop. This would extend laterally from the ridge until the shallower region of melting pinched out, leaving the standard situation represented by Figure 10B.

It is impossible for CO_2-rich vapor to exist in the lower lithosphere of continents. A low value of CO_2/H_2O in vapor is sufficient to produce dolomite (Figs. 5 and 8). The shield geotherm traverses the Do + V surface (or the phlogopite + Do + V surface, Wyllie, 1978, Figs. 12 and 13) close to a vapor contour for $X^V(CO_2) = 0.1$ (Fig. 10D). Warmer geotherms traverse contours for slightly higher $X^V(CO_2)$, but even for the ocean plate geotherm, $X^V(CO_2)$ does not exceed 0.5. Only with upwelling and the development of abnormal temperatures can the geotherm pass above the Do + V buffering surface, and only under these circumstances can vapor develop with higher CO_2/H_2O, if the bulk composition is suitable.

Magma generation

Figures 1, 2, 8, and 10 provide the basis for consideration of magma genesis in the mantle. Our knowledge of the percentages of melting and compositions of liquids within the melting interval of peridotite (Fig. 1) is still inadequate (Wyllie, 1971, p. 194 and 204; Mysen and Kushiro, 1977). Our knowledge of the compositions of liquids on the solidus surface for peridotite–H_2O–CO_2, represented tentatively in Figure 8, is hotly debated. We have little specific information about the compositions and percentages of liquids between the vapor-saturated solidus of Figure 8 and the solidus in Figure 1, as a function of temperature, CO_2/H_2O, and amount of $(CO_2 + H_2O)$.

According to Figure 10, dolomite should be distributed through large volumes of the upper mantle,

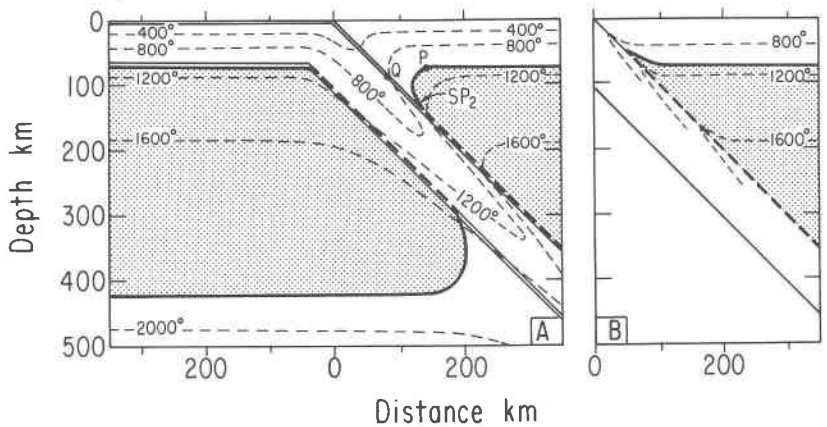

Fig. 11. Cross-section through idealized, 45° subduction zone showing calculated thermal structures (A) slightly modified version of Toksöz *et al.* (1971, Fig. 7), and (B) Oxburgh and Turcotte (1970). The shaded areas show where melting occurs if H_2O is present; the heavy line is the solidus for peridotite–H_2O (see Fig. 2). Points P, Q, and SP_2 are explained in connection with Fig. 13, 16, and 17.

wherever CO_2 is present. I would feel happier about this diagram if there were more occurrences of dolomite in peridotite nodules than the single example reported by McGetchin and Besancon (1973). If we assume that the measured values of about 0.2 percent CO_2 in mid-oceanic basalts represent a 5-fold concentration, then the original mantle source region would have contained 0.04 percent CO_2. This amount of CO_2 would produce less than 0.1 percent modal dolomite, which is not very much in a hand specimen. Figure 10 was drawn for an arbitrary quantity of 0.1 percent CO_2, but the same petrological structure would exist for 0.01 percent CO_2, or even 0.001 percent CO_2.

This raises the question of whether such a small amount of CO_2 or dolomite needs to be considered as a significant component. The answer is "no" for a region of upwelling as in Figure 10C, where extensive melting to generate basalt swamps the trivial quantity of CO_2 and H_2O. For other regions, however, even traces of CO_2 and H_2O cause incipient melting of the mantle, and the presence of a small proportion of CO_2 is sufficient to generate dolomite and buffer the magma composition to subsilicic, alkalic compositions. These CO_2-rich magmas would be enriched also in incompatible elements. Their local development where CO_2 became available, followed by migration or eruption, would surely produce inhomogeneities for many minor and trace elements in mantle peridotite.

The fact that the seismic low-velocity zone is absent or weakly developed beneath continental shields is evidence that H_2O and CO_2 are normally absent in this environment. However, the fact that kimberlites and other alkalic, subsilicic magmas have been erupted through continental lithosphere confirms that CO_2 and H_2O are locally concentrated, from time to time. Walker *et al.* (1978) have calculated that if interstitial magma in the seismic low-velocity zone exceeds about 0.1 percent, the magmas would drain upwards.

The phase diagrams in Figures 7 and 9 show that a liquid migrating upwards from within the low-velocity zone under adiabatic conditions could reach the solidus associated with the maximum, mn, at a depth of about 80 km. At this level, the magma must evolve gases, with high CO_2/H_2O. In a region of tension, the gases could enhance the prospect of crack propagation and explosive eruption of magma and gas (O. L. Anderson, personal communication, 1977).

The influence of volatile components on magmas generated from peridotite also becomes important in subduction zones, where dehydration of the oceanic crust yields hydrothermal fluids. Of particular interest are the parts of Figure 8 for the generation of quartz-normative basalts and andesitic magmas.

Magmas from subducted oceanic crust and overlying mantle

Figure 11 provides the framework for discussion of magma generation in subduction zones. The asthenosphere below the lithosphere is represented by the stippled layer. This is the region within which peridotite with a trace of H_2O would contain traces of liquid (based on a geotherm and phase diagram, Figs. 1 and 2; Wyllie, 1971, p. 132, 135, 363). The oceanic lithosphere is forced through this layer, with depression of the isotherms as shown in Figure 11A. Mechanical disturbances cause frictional heating, and Figure 11B shows one interpretation of how frictional heating along the surface of the subducted slab might raise isotherms, thus promoting magma generation. These

alternatives, and a third one involving convection within the mantle wedge above the subducted lithosphere, will be considered after review of processes and phase diagrams.

The subduction of oceanic lithosphere introduces several additional aspects for magma generation compared with those represented in Figures 8 and 10. There is the introduction of different material into the mantle, the gabbroic oceanic crust, and perhaps some sediments. There is the transportation of volatile components from the hydrosphere into the earth's interior, resulting from reaction between ocean and crust. There is the migration of these volatile components into mantle peridotite, resulting from dehydration of the crust following subduction and heating.

Magmatic products associated with subduction are dominated by the calc-alkaline rock series, basalt–andesite–dacite–rhyolite of volcanic arcs, and gabbro–tonalite–granodiorite–granite of batholiths in continental margin arcs. Possible sources for the magmas in these associations are the subducted oceanic crust, the overlying mantle, and, for the batholiths and some acid lavas, the base of the continental crust.

In order to understand petrogenesis in regions of subduction, we must know the space–time–composition relationships of the magmatic products (*i.e.* the geology and petrology), the thermal structure at depth as a function of time, the geophysical and petrological processes involved, and the phase diagrams for possible source rocks and observed magmatic products through the range of pressure and temperature from deep source to surface, including the effects of variations in content of H_2O. These aspects of petrogenesis are interrelated, but each can be examined independently of the others, to a certain extent.

Whenever I try to apply the results of experimental studies to processes in subduction zones, I conclude that we still lack adequate geological information. Recent papers confirm that others share this concern. Miyashiro (1975) reviewed the island-arc volcanic rock series, stating that "the existing data are so complicated that they are not properly understood and used in the existing discussions, and incorrect generalizations are widespread." Brown *et al.* (1977) described the geochemical complexities of the Lesser Antilles volcanic island arc, and stated that "Island arcs differ appreciably in the composition of their magmatic products, and a unifying hypothesis cannot yet be applied to explain their origins."

The thermal structure is obviously critical for magma generation, and many models have been calculated; two of them are illustrated in Figure 11. Because of the uncertainties in computed thermal structures, Ringwood (1975, p. 195) adopted an approach assuming a level of heating "that leads to a satisfactory petrological model." This approach assumes that the source rocks and processes are known, but there are many competing hypotheses in the literature suggesting that there remain differences of opinion about what constitutes a "satisfactory petrological model."

The processes have not been adequately defined, nor have the phase relationships of the possible materials yet been determined in sufficient detail to provide definitive discriminants among competing hypotheses. One problem is that petrologists think faster than they can complete tedious experiments in pressure vessels. New hypotheses tend to leapfrog ahead of the substantiation of existing hypotheses by reliable phase equilibrium data.

Processes in subduction zones: subductio ad absurdum

Figure 12 summarizes in schematic form many of the processes that have been invoked to explain the origin of magmatic rocks in subduction zones. It illustrates the paths followed by volatile components from source rocks to sites of magma generation.

The box at the lower left represents metamorphosed and metasomatized oceanic crust with local bodies of serpentinite, and thin intercalations of pelagic sediments near the top. With downward movement, greenschists are progressively dehydrated to amphibolite, and amphibolite is converted to quartz eclogite. The serpentinite bodies are dehydrated, producing talc as an intermediate product. Because of the reversed geotherm through the subducted crust (Fig. 11), the rocks of higher metamorphic grade lie above the more hydrated rocks of lower grade. Mica and carbonate in pelagic sediments or metasomatized basalts release H_2O and CO_2.

The hydrothermal fluids released by dehydration reactions are concentrated solutions of uncertain composition. The fluids may initiate melting in the oceanic crust either by diffusion upwards to levels where temperatures are higher, or by transportation to greater depths trapped as inclusions or along grain boundaries. They may diffuse into overlying mantle peridotite where they could persist as fluids, become fixed in hydrous minerals, or initiate melting. They may diffuse down the thermal gradient into the cooler part of the slab, producing minerals such as serpentine and perhaps phlogopite, which could carry H_2O down to deeper levels.

Magma could be generated in the oceanic crust by

partial melting of sediments, or by partial melting of amphibolite or quartz/coesite eclogite, either dry or with fluids. Magma could be generated in overlying mantle if the hydrothermal fluids cross the peridotite–H_2O solidus, if hydrous magma from the subducted crust reacts with the mantle producing pyroxenite or hybrid magmas, or if the hydrous fluids produce metasomatic phlogopite or other hydrous minerals in the peridotite that are subsequently transported by convecting mantle down to melting temperatures. Rising magmas, especially the hydrous magmas generated by fluids, would experience fractionation through the crystallization of minerals that varied as a function of depth.

Figure 12 covers a wide range of possibilities from the concept of a primary magma rising directly from the subducted crust, to a fractionated magma produced from liquid generated in the pyroxenite of hybridized mantle peridotite. All of these processes have been proposed. Could all of them be valid in some circumstances? Or is that too absurd?

Phase relationships of material in subducted crust and overlying mantle

Figure 13 compares three critical phase boundaries for the gabbro constituting the bulk of the oceanic crust, and for the peridotite in the overlying mantle. For each rock, there is a fixed point of intersection

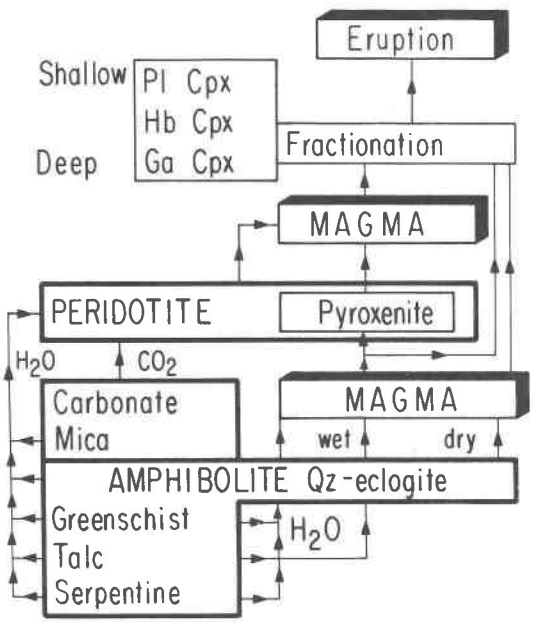

Fig. 12. Processes in subduction zones. Schematic representation of paths followed by H_2O and CO_2 released from source materials in subducted ocean crust, sites of magma generation, and types of fractional crystallization.

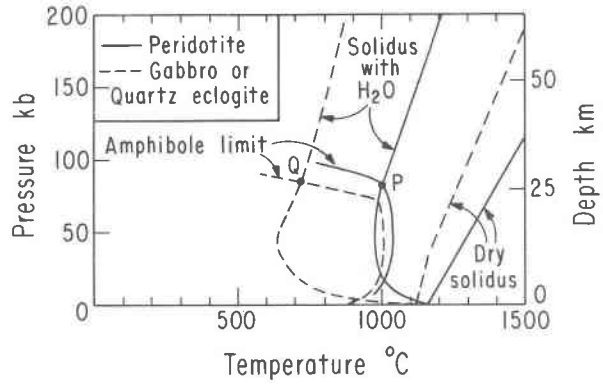

Fig. 13. Selected melting and amphibole dehydration curves for gabbro(quartz–eclogite) and peridotite (Lambert and Wyllie, 1972; Millhollen *et al.*, 1974).

between the amphibole stability limit and the solidus curve in the presence of H_2O. For peridotite, P is located at 25 kbar and 990°C. For gabbro, Q is located at 25 kbar and 725°C. These values for P and Q are adopted here, but remember that they are not uniquely defined. Other investigators working with other rocks have determined different values. Green (1973a) located P at 29 kbar, 1020°C. Mysen and Boettcher (1975) determined several different values for P, one example being near 18 kbar, 850°C.

Serpentine contains 14 percent H_2O, and bodies of serpentinite within subducted oceanic crust may therefore be an important source of hydrothermal fluids. Dehydration curves for serpentine are given in Figure 14. Reaction (1) is for serpentine accompanied by brucite, and reaction (2) is for the dehydration of serpentine itself, producing forsterite and talc. In Figure 15, the dehydration curve for serpentine is extended to the high-pressure field for the stabilization of dense hydrous magnesian silicates (DHMS) that coexist with forsterite + enstatite, according to Yamamoto and Akimoto (1977). Their curve for the dehydration of talc is also drawn.

Chlorite commonly contains 10–12 percent H_2O, amphibole contains about 2 percent H_2O, and amphibolite may contain 1 percent H_2O. The transition zone from greenschist to amphibolite facies in the subducted oceanic crust is therefore another important source region for hydrothermal fluids. The transition from greenschist to amphibolite facies marked in Figure 15 is approximately coincident with the serpentine dehydration curve at depths greater than about 50 km.

According to reactions calculated by Delany and Helgeson (1978), there is a 14A-chlorite stable to higher pressures than amphibole. Experimental studies are required to determine whether or not such a

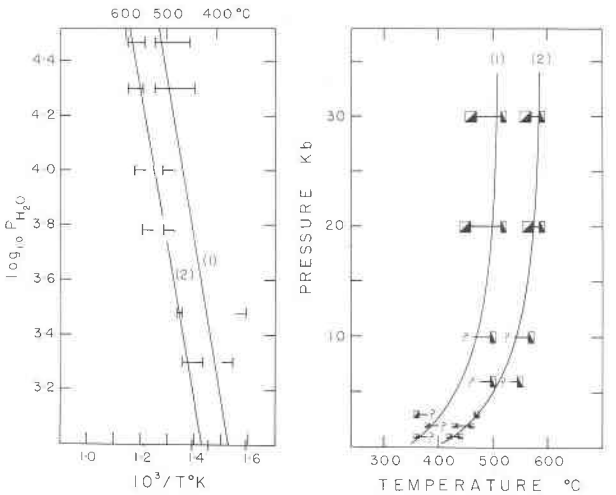

Fig. 14. Dehydration reactions for serpentine: (1) serpentine + brucite = forsterite + vapor, and (2) serpentine = forsterite +talc + vapor, after Scarfe and Wyllie (1967, unpublished manuscript). Points are for runs with the mineral-assemblage starting mixtures (either reactants or products) which showed significant or complete reactions—each box is therefore one half of a reversal pair (not all pairs could be completed). Results to 3 kbar from Scarfe and Wyllie, and at higher pressures from run table of Kitahara *et al.* (1966). The best straight lines through the brackets in the left-hand diagram were replotted as curves in the *PT* diagram.

chlorite can occur in bulk compositions corresponding to gabbro and peridotite at depths greater than 100 km and to temperatures higher than 700°C. It is not yet established whether hydrous minerals other than phlogopite can persist into this region (Wyllie, 1973, 1979); epidote and hydrogarnet are two possible candidates.

Thermal structure and dehydration

The thermal structure of a descending slab is not known. Two of four published models that were compared by Wyllie (1973) are represented in Figure 11, and, for these models, the estimated temperatures occurring across the 5 km thickness of subducted crust are compared in Figure 15. The wide band calculated by Oxburgh and Turcotte (1970), including frictional heating, corresponds to high temperature gradients across the crust, whereas temperature gradients are much lower across the narrow band computed by Toksöz *et al.* (1971).

Hasebe *et al.* (1970) suggested that frictional heating associated with subduction (Fig. 11B) was cancelled out by heat absorbed in dehydration reactions down to 60 km depth. Anderson *et al.* (1976) evaluated quantitatively the heat absorbed in dehydration, concluding that the isotherms were lowered in subducted ocean crust and the overlying mantle wedge. Delany and Helgeson (1978) calculated dehydration reactions relevant to subduction zones to 100 kbar, and the changes in enthalpy and volume for each reaction. Using these parameters, Anderson *et al.* (1978) evaluated the relative importance of shear stress heating and the heat sink created by dehydration reactions. They concluded that frictional heating is not an important heat source for magma generation in older arcs.

According to Anderson *et al.* (1978), dehydration reactions proceeding through 50 m.y. in the depth interval 75–125 km (compare Wyllie, 1973; Delany and Helgeson, 1978) cool the oceanic crust to very low temperatures, as shown by the temperature band for 5 km thickness in Figure 15. Isotherms calculated for the overlying mantle wedge were considerably lowered compared with those plotted in Figure 11A. Anderson *et al.* (1978) stated that inclusion of asthenospheric convection would increase the heat flow into the slab by less than 10 percent. Given the two thermal structures OT and TMJ and the dehydration reactions plotted in Figure 15, the subducted oceanic slab would be completely dehydrated by a depth of 120 km. Given the thermal structure calculated by Anderson *et al.* (1978), the slab is dehydrated by a depth of about 185 km (last talc at the base of the slab). Serpentine dehydrates between about 140 and 155 km, and talc reacts between about 165 and 185 km. Water can be carried deeper only if phlogopite is generated in the crust (Wyllie, 1973, 1979; Fyfe and McBirney, 1975), or if other hydrous minerals turn out to have stability fields above 30 kbar and 750°C (preceding section).

Ringwood (1975, p. 295) proposed that serpentinite disproportionates into DHMS, which constitutes an important host for H_2O in the sinking lithosphere down to depths as great as 300 km. Even for the coolest of the three subducted oceanic crusts represented in Figure 15, serpentine and talc are completely dehydrated before the pressure becomes high enough to stabilize DHMS minerals. These minerals can serve as storage sites for H_2O only if H_2O is present where they become stable. According to the data available at present, dense hydrous magnesian silicates are not likely candidates for deeper transportation of H_2O, unless serpentine is present in peridotite deep within the subducted lithosphere.

Conditions for dehydration

The processes of dehydration and melting in and above a subducted slab are commonly described in qualitative terms, without too much attention to specific phase diagrams, temperatures, and pressures. In

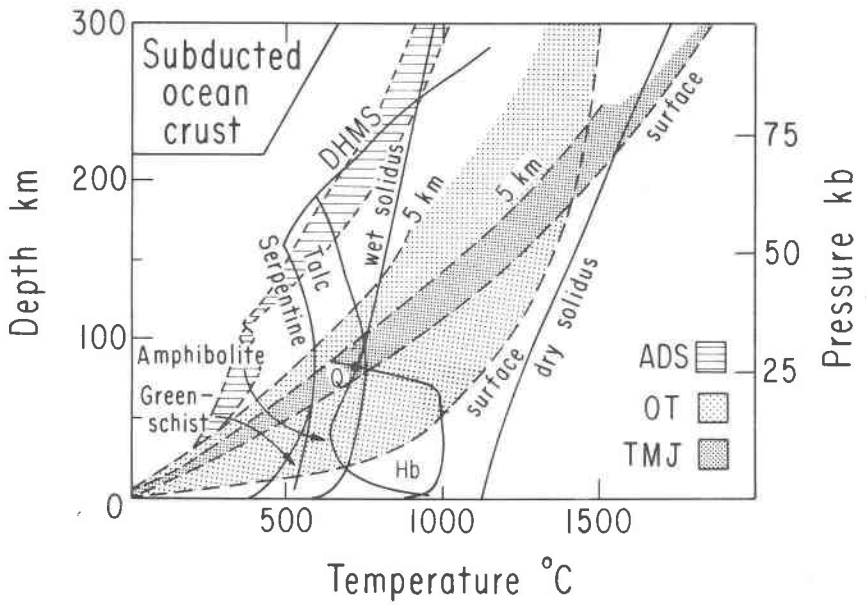

Fig. 15. Temperature distributions, dehydration reactions, and melting reactions in subducted ocean crust composed of gabbroic rocks enclosing bodies of serpentinite. The shaded bands give temperature distributions across a 5-km-thick subducted crust according to three investigations discussed in the text. Serpentinite reactions are represented by serpentine, talc, and DHMS dehydration. The transition from greenschist to amphibolite facies is indicated. The fusion and amphibole curves are from Fig. 13.

order to test the processes summarized in Figure 12, it is necessary to combine the thermal structure of a subduction zone with the phase relationships of the materials. There are many difficulties associated with this exercise, including the following. The angle of dip may vary from one slab to another, and even from shallow to deeper levels for a single slab. There is no unique and complete solution for the thermal structure (Figs. 11 and 15). There is a variety of phase diagrams to choose from, even for the three basic reactions given in Figure 13.

Wyllie (1973) used experimentally-determined reactions and the two thermal models of Figure 11 to map dehydration fronts for serpentine, talc, amphibole, and phlogopite, occurring within gabbro and peridotite, and for muscovite in sediment. The boundaries for the dehydration of serpentine (SG_1–SG_2) and amphibole (H_1–H_2) in the crust are given in Figure 16, and for amphibole in overlying mantle (H_3–H_4) in Figure 16A. For both thermal models, most hydrous minerals are dehydrated before they reach a depth of 100–120 km (or at most 150 km if biotite and phlogopite are present). Delany and Helgeson (1978) presented dehydration fronts based on calculations for simple minerals, with similar results. Anderson *et al.* (1978) described dehydration of the crust within the depth interval 80–125 km, but their calculated temperature distribution in Figure 15 indicates that after 50 m.y. of subduction, serpentine and talc may reach depths of about 150 km and 180 km, respectively.

It is difficult to illustrate details of dehydration and melting processes in diagrams drawn to scale as in Figure 16. Moreover, the uncertainty of thermal models makes it difficult to be specific about depths and temperatures. Figure 17 is a schematic model which permits examination of processes, unencumbered by the need for precise temperatures and depths. Figure 17A represents both crustal models of Figure 16, with all reaction curves in their correct relative positions with respect to pressure and temperature. The curve $T_1T_2T_3$ is for dehydration of talc. The points P and Q (from Fig. 13) have defined pressures and temperatures, giving the depth 85 km as the only fixed point on the vertical scale.

The reaction curves may rotate around Q, and they may extend through a large or small depth interval, depending upon the thermal structure, as shown by Figures 16A and B. The points Q and P are situated on the isotherms for 725° and 990°C, respectively. They may move horizontally in the diagram for different thermal structures. If the slab is cool enough, point Q may be displaced through the upper edge of the crust, as in Figure 17B. Under these circumstances, amphibole dissociates (H_1–H) before the solidus (SE–SE_2) is reached. For Figure 17B to correspond to the very cool model of Anderson *et al.* (1978), the serpentine reaction curve SG_1–SG_2 would

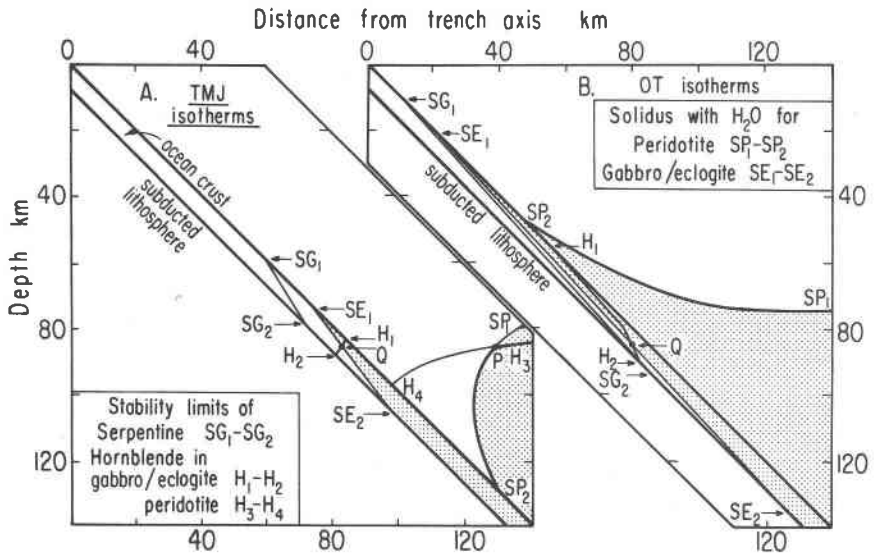

Fig. 16. Petrological structure of the subducted ocean crust, according to the phase boundaries in Figs. 2 and 15, and temperature distributions in (A) Fig. 11A, and (B) Fig. 11B. The shaded areas show the regions of potential melting in subducted crust and overlying mantle, if H_2O is available.

be located at depths considerably greater than the amphibole dehydration curves, H_1–H and P–H_4. In fact, according to Figure 15, the subducted ocean crust would remain in the greenschist facies and not reach the metamorphic grade of amphibolites.

Conditions for melting

The shaded areas in Figures 16 and 17 show the regions of potential melting, if there is any H_2O available, at temperatures above the solidus boundaries for gabbro (quartz eclogite)–H_2O, SE_1–SE_2, and peridotite–H_2O, SP_1–SP_2. The boundaries H_1–Q and H_3–P mark the solidus for amphibole-bearing rocks without free H_2O (compare Figs. 2 and 13).

For the arrangements shown in Figures 16 and 17A, with Q situated within the subducted crust, magma is generated by the direct melting of amphibolite (H_1–Q), and by migration of H_2O from the serpentine, greenschist, and talc dehydration boundaries across the solidus for amphibolite and quartz eclogite, SE_1–SE_2. The sites of magma generation may be limited to a relatively narrow depth interval, as in Figure 16A, or they may extend through a wider interval, as in Figure 16B.

For the arrangement shown in Figure 17B, with Q displaced through the upper edge of the crust, amphibolite dissociates before it melts, and magma is generated at greater depths as H_2O from dehydration of serpentine and talc (SG_1–SG_2, T–T_3) crosses the solidus for quartz eclogite, SE–SE_2. This is the model preferred by Nicholls and Ringwood (1973). According to the model of Anderson *et al.* (1978), the solidus SE–SE_2 is located at depths well below the dehydration boundaries, and the subducted ocean crust does not melt at all.

For a model with crust and mantle warmed by friction, as in Figures 11B and 16B, hydrothermal fluids released from the crust would cause melting in the overlying peridotite at depths between about 50 and 100 km, unless the fluids were trapped first in the crustal melts produced along SE_1–SE_2.

For a warm model without significant frictional heating, represented by Figures 17A and 16A, fluids released from the crust would not cause melting in the overlying peridotite, because they would not pass through the area SP_1–P–SP_2. Up to a limit of 0.4 percent, H_2O could be fixed in the peridotite as amphibole, and if potassium is transported in solution phlogopite could also be produced. If part of the mantle adjacent to the subducted crust moves down in asthenospheric convection, then the amphibole peridotite would dehydrate as it was carried across the boundary P–H_4. Perhaps some of this fluid could be trapped as inclusions or along grain boundaries to generate some liquid as it was transported across the solidus P–SP_2, but the amount of H_2O involved in the melting reaction would surely be small. If phlogopite was produced, this could be carried to greater depths until it crossed the boundary Ph in Figure 17A, marking the position for vapor-absent melting of phlogopite–peridotite.

The arrangements in Figures 16A and 17A could

be modified in two ways that might permit the generation of magma by passage of fluids from the crust into the area SP_1–P–SP_2 of the mantle. A higher temperature gradient within the crust could rotate the curves around Q and extend the serpentine stability to greater depths, so that SG_1–SG_2 would pass below the area SP_1–P–SP_2. Alternatively, if the overlying mantle were hotter than in Figure 11A, P would move closer to the surface of the subducted slab (with no change in depth), and overlap between crustal dehydration reactions and mantle melting would be produced. Neither of these modifications would be very effective, however, because H_2O released from serpentine and talc would have to pass through the region for potential melting of quartz eclogite, and it would dissolve in the crustal magmas before making its way into the overlying peridotite.

For the model of Anderson *et al.* (1978), where the solidus of subducted crust is located much deeper than the dehydration fronts, the magmas must be generated in mantle peridotite, through "convection of asthenosphere above the slab and lowering of the melting point of overlying peridotite by release of water from dehydration of the subducted oceanic crust." Figure 17B can be used to examine the consequences of this model. First, the solidus SE–SE_2 in Figure 17B is removed from consideration (see Fig. 15). According to Figure 15, after 50 m.y. of subduction, the oceanic lithosphere driving downwards into the mantle is releasing H_2O from serpentine and talc within the two depth intervals 140–155 km and 165–185 km. According to Figure 2 of Anderson *et al.* (1978), vertical movement of these fluids would not carry them across the boundary P–SP_2 and into the mantle melting region. If magmas are to be generated, the mantle must be much hotter than indicated in the calculated models, and the point P must be moved significantly closer to the surface of the slab. According to the calculations of Andrews and Sleep (1974), it appears that this could be accomplished by convective motion in the overlying mantle, induced by the downgoing slab.

Andrews and Sleep (1974) calculated idealized models confirming the feasibility of induced flow as a working hypothesis. They considered flow in the wedge between the slab and the lithosphere of an island arc, corresponding to the right-hand shaded area in Figure 11A, or the shaded mantle areas in Figures 16 and 17. Their solutions showed upwelling and heating behind the arc, the development of large stresses in the corner near PQ with local heating and magma generation (although temperatures indicated

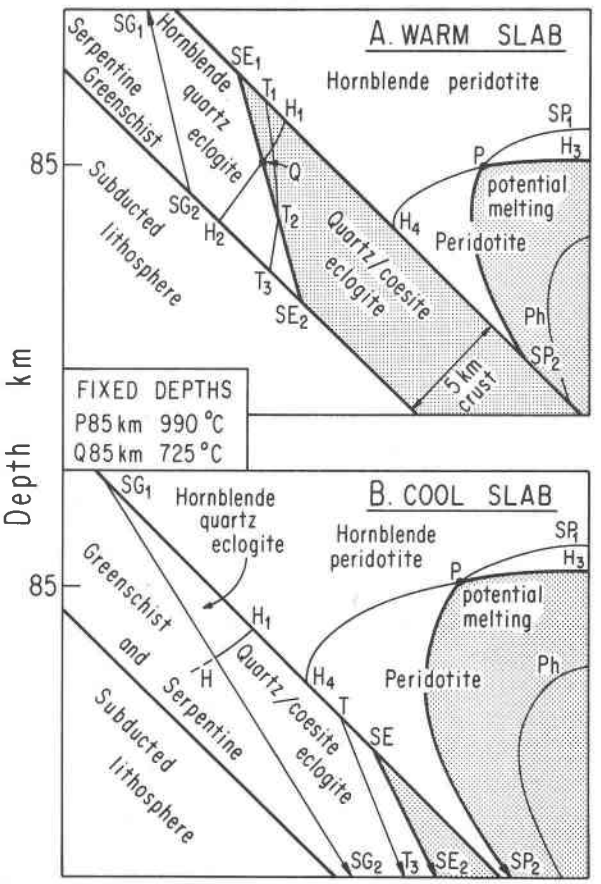

Fig. 17. Schematic representations of subducted ocean crust, showing the correct relative positions of reaction boundaries, according to different thermal models. Boundaries are identified in Fig. 16, except for $T_1T_2T_3$ which is dehydration of talc (Fig. 15). Points P and Q occur at fixed depths and constant temperature (see Fig. 13). They may therefore move horizontally, according to the distribution of isotherms. In the cool slab of diagram B, the point Q has passed through the upper edge of the slab, thus passing out of existence.

would not permit melting of peridotite without access of H_2O), and the entrainment of island-arc lithosphere by the downgoing slab. This produces very high temperature gradients in the mantle overlying the subducted slab. For the very cool slab temperatures calculated by Anderson *et al.* (1978), the temperature gradients in the mantle adjacent the subducted slab must be very high if the solidus SP_2–P is to be located in a position suitable for the generation of magmas from the fluids of dehydration. In fact, it should be possible to sketch isotherms required for magmas to be generated in suitable locations, and to test these against geophysical parameters.

Figures 16A and 17A represent models where hydrous magmas are generated from oceanic crust at

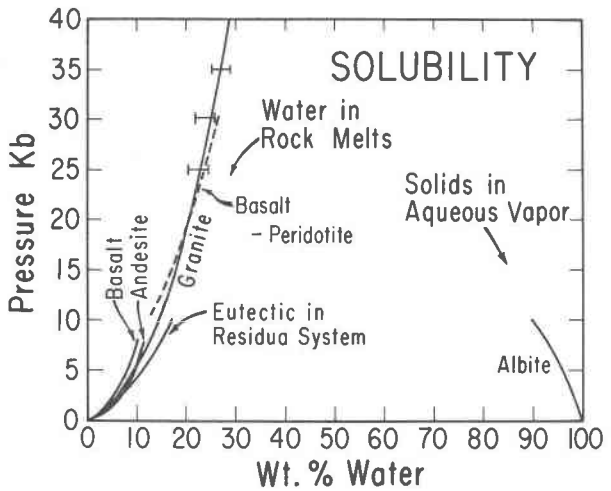

Fig. 18. Solubility of H_2O in magmas, after Stern and Wyllie (1973a), with curve for basalt–peridotite according to Green (1973b).

depths corresponding closely to amphibolite dehydration or melting. It is anticipated that such magmas would have intermediate SiO_2 contents (Green, 1972; Stern, 1974; Stern and Wyllie, 1978; Allen and Boettcher, 1978). They are not likely candidates for primary andesite magmas, however, because their temperatures are in the range 700–800°C (Fig. 13), much lower than those of erupted andesites.

Hydrous magmas generated from quartz eclogite as in Figure 17A are unlikely to reach temperatures of 1,000°C (Fig. 15), but they do have the prospect of rising into warmer mantle across the line SP_2–P where peridotite can melt if H_2O is present. This process is related to the hybridization scheme of Nicholls and Ringwood (1973).

Now consider the compositions of liquids produced by the flow of fluids into the area SP_2–P–SP_1 of the mantle. Figure 8 illustrates the composition of near-solidus liquids from peridotite–H_2O as a function of pressure, corresponding to melts produced along the line SP_1–P–SP_2 in Figure 17. The point P in Figure 17 corresponds to B in Figure 8A, which is near Z in Figure 8C (compare Figs. 4, 8, and 13). H_2O-saturated liquids developed near the solidus P–SP_2 in Figure 17 are therefore nepheline–forsterite-normative. These are not likely parents for the calc-alkaline series basalt–andesite–dacite.

According to Figure 8, the flow of hydrothermal fluids into mantle peridotite can produce hydrous olivine tholeiites directly only if the isotherms in the mantle are elevated to such an extent that the attitude of the line P–SP_1 in Figure 17 is reversed, so that fluids rising from the region H_1 pass directly across the boundary P–SP_1. H_2O-saturated near-solidus liquid for the solidus P–SP_1 ranges from forsterite-normative (ZY in Fig. 8C) to quartz-normative (Y in Fig. 8C) if Sp_1 is as shallow as about 65 km. In order to produce andesites directly from mantle peridotite, according to Figure 8C, it would be necessary for the line SP_2–P–SP_1 to rise to shallow levels, with asthenospheric convection elevating mantle temperatures to 1,000–1,100°C at a depth less than 40 km.

The liquids produced near the solidus where fluids migrate into the area SP_2–P–SP_1 are saturated with H_2O. According to Figure 18, saturated basic and acid magmas contain 20–25 weight percent dissolved H_2O in the depth interval 70 to 100 km. If there is a large flux of H_2O across the solidus boundary, a zone of H_2O-saturated liquid may extend into the area SP_2–P–SP_1 with increasing temperature. Alternatively, with increasing temperature within the zone, the liquid developed may be H_2O-undersaturated.

The H_2O-saturated liquid generated along the boundary SP_2–P must traverse the region of potential melting en route to the surface. Is equilibrium maintained between liquid and host crystals through all or part of the region SP_2–P–SP_1 in Figure 17, with the liquid composition changing from forsterite–nepheline-normative towards quartz-normative as it rises? Or does the H_2O-rich liquid escape from its crystalline host a short distance above SP_2–P and rise toward the surface as a body of magma independent of its host (Marsh, 1978)? These are questions that merit more attention than they have received.

The high solubility of albite in aqueous vapor at 10 kbar (Fig. 18) supports the suggestion of Fyfe and McBirney (1975) and Anderson *et al.* (1978), and many others, that hydrothermal fluids expelled from

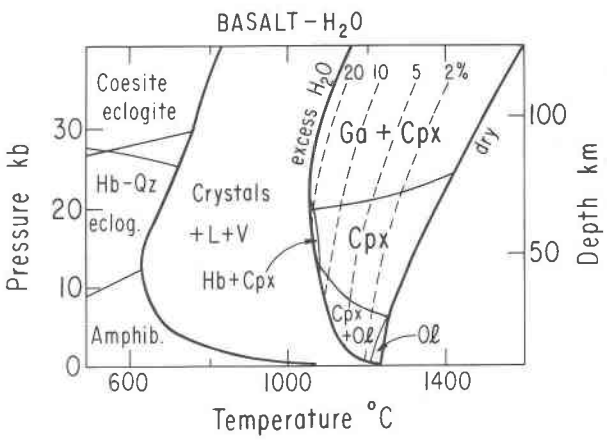

Fig. 19. Phase relationships for basalt–H_2O, modified after Stern *et al.* (1975).

subducted ocean crust may transport many elements into the mantle, enriching peridotite source rocks in the components that give island-arc volcanic rocks their distinctive geochemistry.

Phase relationships of basalt–andesite–rhyolite–H_2O

In order to trace the paths of liquid compositions from magma sources at depth to the observed magmatic products at or near the surface, we need more complete phase equilibrium data than the fragmentary information presently available. Figures 19–24 outline a phase-equilibrium framework in terms of P–T–$X(SiO_2)$–$X(H_2O)$ for three individual compositions with H_2O, representing basalt, andesite, and rhyolite, and for the calc-alkaline series, basalt–andesite–rhyolite, with H_2O.

Stern *et al.* (1975) combined new experimental data for three rocks with previously published experimental data on the same rocks to construct phase diagrams with excess H_2O to 35 kbar, and the three H_2O-undersaturated liquidus surfaces, mapped with liquidus or near-liquidus minerals. The results are combined in Figures 19–21. For details of the phase boundaries within the H_2O-excess crystallization interval, and of the previously published data on these compositions, see Stern *et al.* (1975). The H_2O solubilities in Figure 18 correspond to the values along the liquidus curves for excess H_2O in Figures 19–21.

Stern and Wyllie (1973b, 1978) discussed the use of these three compositions as a representation of the calc-alkaline series in terms of a single composition join through a complex rock system. They combined data from the three rocks to illustrate phase relationships in the series basalt–andesite–rhyolite–H_2O at 30 kbar, including crystallization through the H_2O-undersaturated region. Huang and Wyllie (manuscript in preparation) have similar data at 15 kbar. Figures 22–24 are an extension of this approach, covering the same composition join from 1 bar to 35 kbar, and for H_2O contents of 0 percent, 5 percent, and sufficient to saturate (excess). The task of patching together the widely-spaced information from only three compositions (Figures 19–21) was facilitated by examination of other experimental data for calc-alkaline rocks, including especially the results of Green and Ringwood (1968, 1972), Green (1972), Eggler (1972), Nicholls and Ringwood (1973), Allen *et al.* (1975), and Allen and Boettcher (1978).

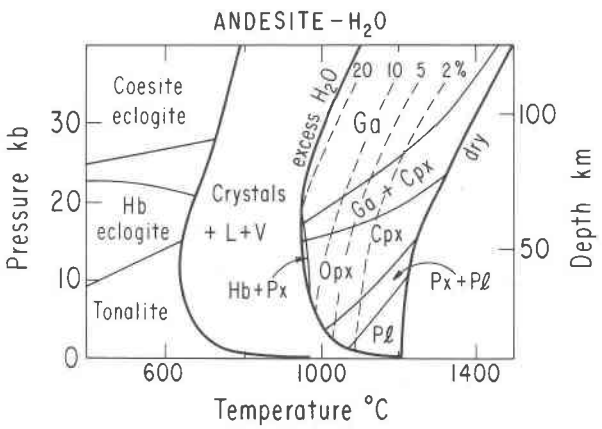

Fig. 20. Phase relationships for andesite–H_2O, modified after Stern *et al.* (1975).

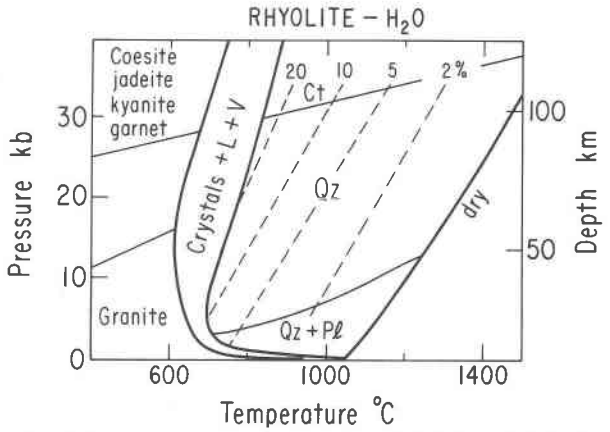

Fig. 21. Phase relationships for rhyolite–H_2O, modified after Stern *et al.* (1975). See also Huang and Wyllie (1973).

Figure 22 is a schematic map of the dry liquidus surface for the calc-alkaline rock series, showing estimated isotherms and liquidus or near-liquidus minerals. This surface connects the dry liquidus lines from Figures 19, 20, and 21. There is an obvious separation into the low-pressure surface, with liquidus temperature decreasing from basic to acid composition, and the high-pressure surface with a temperature trough associated with the field for primary garnet, between the fields for quartz and eclogitic minerals. The regular temperature variation indicated at low pressures is a simplification, because the liquidus temperatures of some dacites at 1 bar are higher than those of andesites and rhyolites on either side (Brown and Schairer, 1971).

Figure 23 shows the marked effect of 5 percent H_2O. This liquidus surface, connecting the 5 percent contours in Figures 19–21, is H_2O-saturated to about 2 kbar. The main changes compared with the dry liquidus are a decrease in area of the primary plagioclase field, the occurrence of orthopyroxene as a near-liquidus phase (within an undefined area), a very large expansion of the field for primary garnet at the

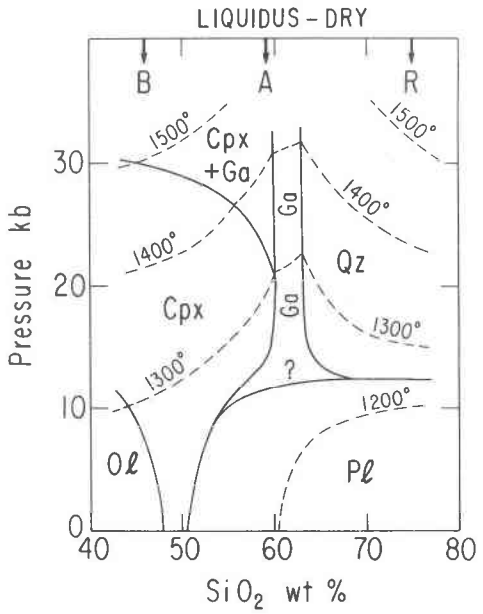

Fig. 22. Phase relationships for the join basalt–andesite–rhyolite–H_2O. The dry liquidus surface, with isotherms and primary crystallization fields. Partly schematic.

expense of clinopyroxene and of quartz, and extension of the field for primary quartz from high pressures to low pressures. There is a well-defined thermal minimum on the surface close to rhyolite compositions at all pressures.

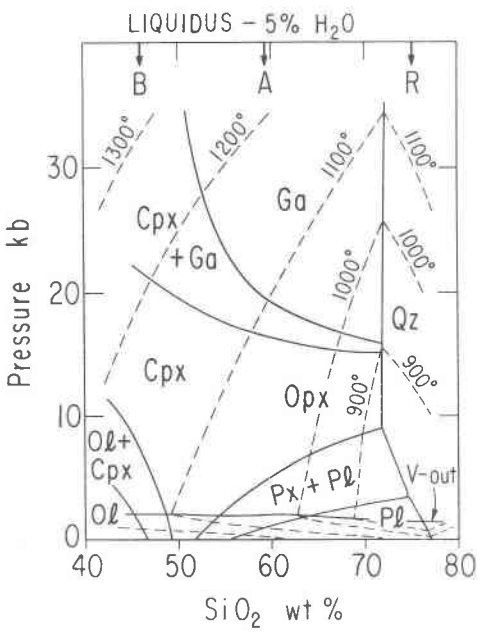

Fig. 23. Phase relationships for the join basalt–andesite–rhyolite–H_2O. The liquidus surface with 5 percent H_2O. Partly schematic.

The general pattern is similar in Figure 24 for excess H_2O, with lower liquidus temperatures, and the addition of amphibole as a liquidus mineral across most of the composition join along with pyroxenes. The area of overlap between garnet and amphibole (see Figs. 19–21) has not been drawn. There is a pronounced temperature minimum on the liquidus surface corresponding to rhyolite compositions in the 5–10 kbar range (compare Fig. 21).

The petrogenetic applications of parts of these diagrams in relationship to the partial fusion of subducted crust (Fig. 19) and mantle peridotite (Figs. 1 and 2), and whether the liquidus mineralogy of various magmas with different H_2O contents (Figs. 19–24) can be matched with the subsolidus mineralogy of possible source rocks (Figs. 1, 8, and 19), have already been discussed at length (*e.g.* Green and Ringwood, 1968; Green, 1972; Nicholls and Ringwood, 1973; Stern and Wyllie, 1973b; Stern *et al.*, 1975).

Stern and Wyllie (1978) combined new data with the results of Green and Ringwood (1968) and Green (1972) to determine the effects of bulk composition, pressure, and H_2O on the compositions of liquidus garnets and pyroxenes at 30 kbar, and they extended by calculation the near-liquidus experimental data right through the crystallization intervals of basalt

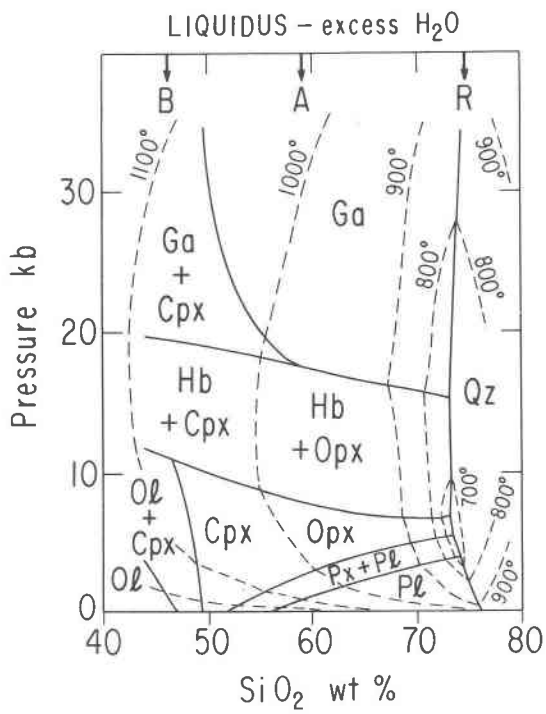

Fig. 24. Phase relationships for the join basalt–andesite–rhyolite–H_2O. The liquidus surface with excess H_2O, H_2O-saturated liquids. Partly schematic.

and andesite, with various H_2O contents. Wyllie (1979) compared the mineral crystallization paths through basalt with the liquidus mineralogy of andesite as a function of H_2O content, and was unable to find a match to support the thesis that andesite may be a primary magma from subducted crust at 100 km depth.

The schematic phase diagrams given in Figures 19–24 can only be rendered complete when details of the phase boundaries have been confirmed, and when the compositions of coexisting liquids and minerals have been determined through the whole range of P, T, and $X(H_2O)$. These data are needed to test the proposed processes of origin of magmas, as well as the products of fractionation outlined in Figure 12.

Magmas from continental crust

The dominant rocks of the deep crust consist of the calc-alkaline plutonic series and their metamorphic equivalents, together with metamorphosed shales and greywackes, of mineralogy similar to that of the plutonic rocks. For most of these rocks in the presence of aqueous pore fluids, melting begins at moderate temperatures, and the migmatitic products are observed in rocks of amphibolite grade. In a recent review of experiments related to crustal anatexis (Wyllie, 1977b), I examined the phase relationships in Figures 19–21 up to 15 kbar, and constructed isobaric sections at 10 kbar through the series shown in Figures 22–24.

Figure 25 illustrates the phase relationships at 10 kbar for the complete series with excess H_2O, and the H_2O-undersaturated liquidus surface with H_2O-content contours and boundaries for the fields of primary crystallization of liquidus minerals. The excess-H_2O relationships connect the fields labelled "crystals+L+V" in Figures 19–21, and the liquidus surface connects the 10 kbar intersections in the same figures. The contours in Figure 25 for the liquidus dry, with 5 percent H_2O, and with excess H_2O, correspond to 10 kbar intersections across the liquidus surfaces in Figures 22, 23, and 24, respectively. Note the steep slope on the liquidus surface between granodiorite and granite compositions, particularly for high H_2O contents.

The small amount of H_2O available in pore fluids during metamorphism is insufficient to saturate the liquids produced by fusion except very close to the solidus. In order to follow paths of fusion and crystallization in the crust, we need diagrams for H_2O-undersaturated conditions. Wyllie (1977b) constructed a slice through the series in Figure 25 for H_2O content of 2 percent. Figure 26 is another slice through Figure 25, for fixed $X(SiO_2)$ corresponding to a muscovite–granite, showing the effect of $X(H_2O)$ on the phase relationships. Figure 26B is an estimate of the percentage of liquid present through the melting interval.

If the temperature rises high enough, and if aqueous pore fluid is present, most rocks in the earth's crust would begin to melt within a rather narrow temperature interval (Figs. 19–21, and 25). The temperature of beginning of melting is independent of the amount of fluid present (Fig. 26), and all H_2O is dissolved within a few degrees of the solidus. If there is only enough H_2O present to constitute hydrous minerals, then vapor-absent melting begins at somewhat higher temperature, as illustrated in Figure 26 where muscovite breaks down in a melting reaction.

For rocks with less than 2 percent H_2O, the melting or crystallization interval is very wide (Fig. 25). This is true even for granite, as shown in Figure 26, despite the fact that granite with excess H_2O melts through a narrow temperature interval, and is therefore commonly regarded as a eutectic-like magma. H_2O-undersaturated liquid of granitic composition can coexist with quartz and feldspar through several hundred degrees. Applications of Figures 25, 26, and related phase diagrams were reviewed by Wyllie (1977b, 1977c).

A small amount of CO_2 could dissolve along with H_2O in granitic magmas at depth but, with uprise and crystallization, the CO_2 must be progressively evolved, because of its low solubility. Exsolution of CO_2 must be accompanied also by transfer of H_2O from liquid to vapor, as illustrated by Wyllie and Tuttle (1960) and Wyllie (1974, p. 466), despite the fact that H_2O may be present in amounts far less than saturation values (Fig. 18). Holloway (1976) has examined the consequences of this exsolution for the evolutionary history of granitic magma rising through the crust. He concluded that the presence of a vapor phase (caused by the CO_2) is likely to exert a significant influence on the activity of H_2O, the phase equilibria, and the physical properties of the magma. He suggested that many of the textural, structural, mineralogical, and geochemical features of granitic rocks could be influenced by differences in the relative abundances of CO_2 and H_2O in the source regions.

Fugitive components of magmas

In the preceding phase diagrams, H_2O and CO_2 have been the only volatile components considered.

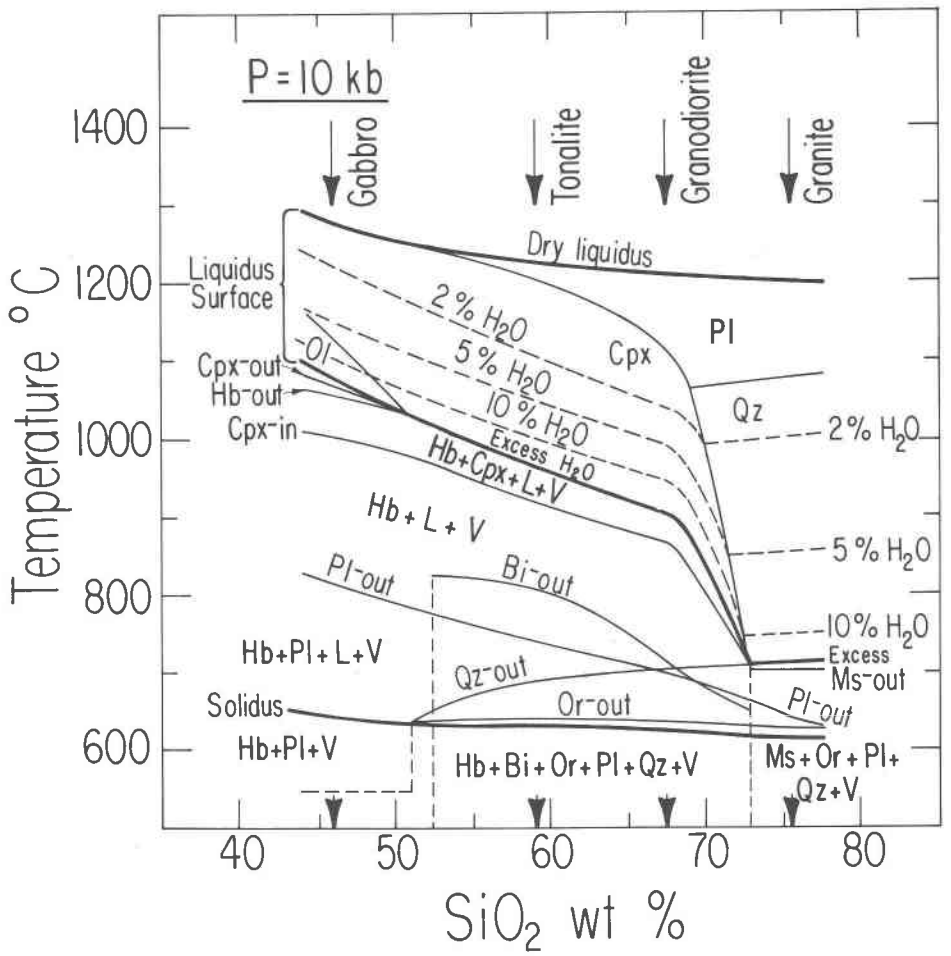

Fig. 25. Phase relationships at 10 kbar for the join gabbro–tonalite–granodiorite–granite–H_2O, chemically equivalent to the join basalt–andesite–rhyolite–H_2O. Partly schematic (Wyllie, 1977b, Fig. 12). Note the arbitrary subsolidus boundaries limiting the ranges of mineral assemblages. The H_2O-undersaturated liquidus surface is contoured by dashed lines for constant H_2O contents.

The experimental results demonstrate that these components may exert a remarkable influence on temperatures and paths of crystallization. There are other fugitive components in magmas that escape, for the most part, during crystallization. Their description as "mineralizers" suggests that these also are influential. I take this opportunity to present unpublished data on the effect of the mineralizer HF, which were obtained in 1957–1958 with the experimental guidance of O. F. Tuttle, and then buried in a file as we became preoccupied with melting experiments in carbonate systems.

Wyllie and Tuttle (1959, 1960, 1961, 1964) investigated the effect of solutions of HF, HCl, NH_3, P_2O_5, SO_3, and Li_2O on the melting temperatures of granite and albite (Ab). Experimental results were obtained initially at 2.75 kbar for mixtures composed of 50 weight percent of solutions, a large excess. For the system Ab–H_2O–HF, we traced the phase relationships from the vapor-excess region into the vapor-absent region, which provided fixes on the compositions and temperatures of liquids that are simultaneously saturated with H_2O and HF.

The system $NaAlSi_3O_8$–H_2O–HF at 2.75 kbar

The starting materials, equipment, method, and the problems of attainment and recognition of an equilibrium phase assemblage were described by Wyllie and Tuttle (1961). The compositions of solutions used are given in Figure 27. The phase fields intersected by the composition join BDEC with excess vapor were published (Wyllie and Tuttle, 1961). Figures 28, 29, and 30 show the phase fields intersected by the composition joins AB, AD, and AE, respectively.

Two phase boundaries were located for the join

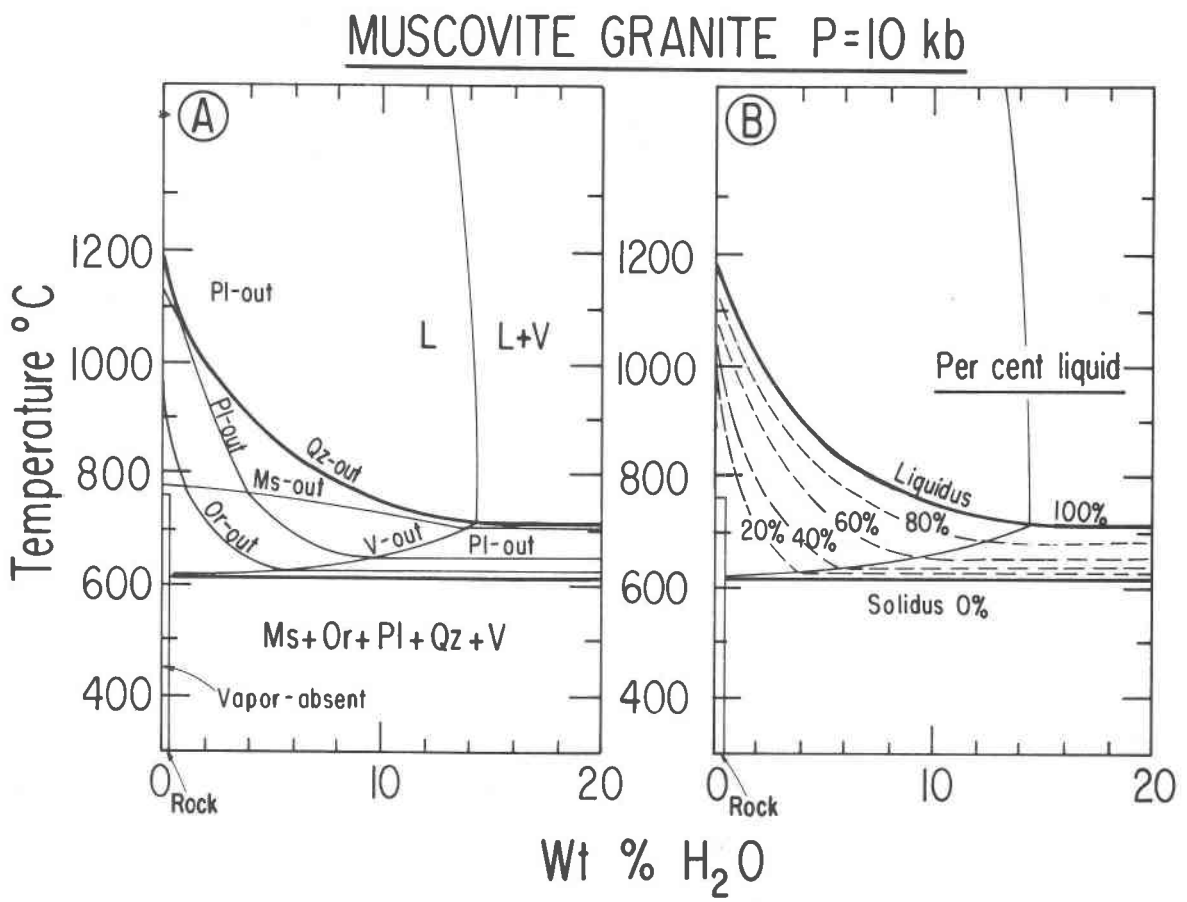

Fig. 26. Schematic diagrams showing the effect of H_2O at 10 kbar on the phase relationships for muscovite–granite (Wyllie, 1977b, Fig. 10). (A) Phase fields. (B) Percentages of liquid within the melting interval from Piwinskii (1973, Fig. 6) for excess vapor, and estimated in vapor-absent area (there is considerable variation possible in the curvature of the contours).

Ab–H_2O (Fig. 28). The solidus for the three-phase assemblage Ab + L + V at 808°C (for discussion of the melting interval, see Wyllie and Tuttle, 1961) is intersected by the steep boundary between fields for Ab + L and L. The point F defines the solubility of H_2O as 8.5 percent. This is high compared with the value interpolated from the results of Burnham and Jahns (1962), 7.6±0.2 percent, but the experimental bracket of about ±1 percent in Figure 28 extends to their value.

The phase fields intersected by the join AD (Fig. 27) are given in Figure 29. The point G is a piercing point for the ternary liquidus field boundary, giving the composition of the liquid that coexists with albite and vapor. Liquid G contains 9.6 percent of dissolved volatile components. The size of albite crystals increases as the proportion of vapor increases. The phase relationships appear to remain ternary (although there is no guarantee that liquid and vapor

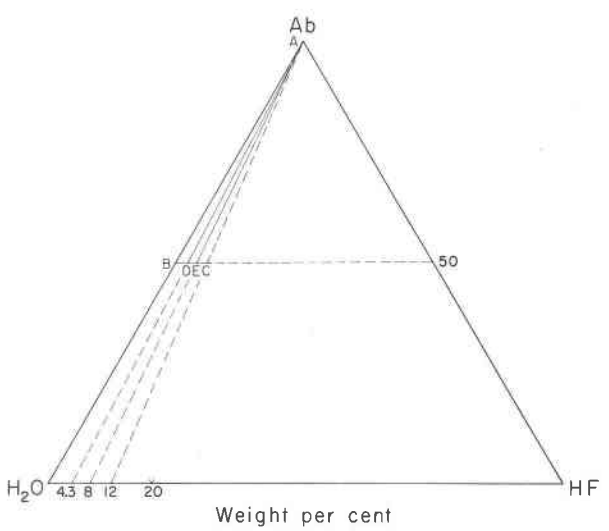

Fig. 27. Composition joins studied in the system $NaAlSi_3O_8$–H_2O–HF.

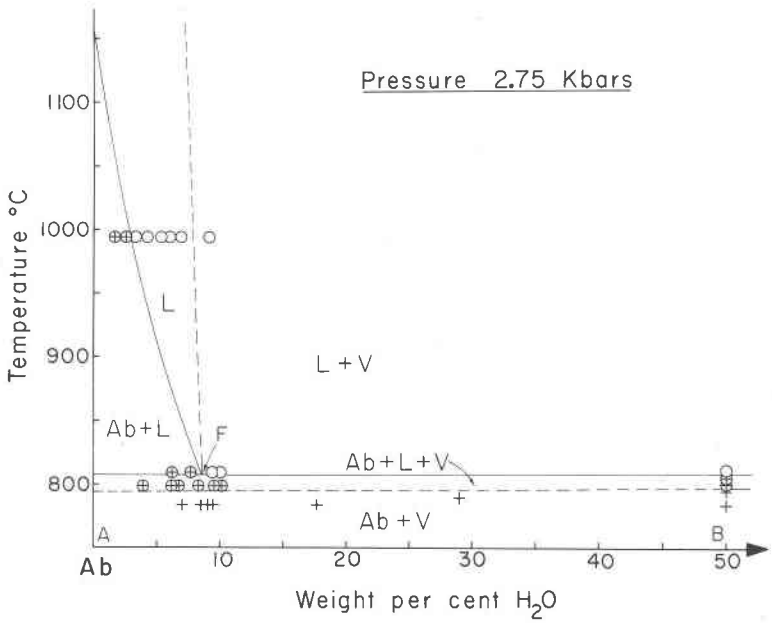

Fig. 28. The system Ab–H_2O at 2.75 kbar (Wyllie and Tuttle, 1959, unfinished manuscript).

phase compositions remain on the triangular join Ab–H_2O–HF), except for the subsolidus run with 50 percent solution, where quartz is produced.

The phase fields intersected by join AE (Fig. 27) are given by Figure 30. The piercing point H represents a liquid with 10.2 percent dissolved volatile components. The near-liquidus phase relationships remain ternary with up to 40 percent solution, but quartz is produced throughout the melting interval for runs with 50 percent solution.

Figures 28, 29, and 30 are superimposed in Figure 31, with the experimentally-determined parts of the sections extended by dashed lines to conform to the geometry of a ternary system (Wyllie and Tuttle, 1960). Extension of the liquidus boundaries to the vapor side does give reasonable intersections with the solidus lines, despite the fact that the vapor-rich compositions are not ternary, as shown by the production of quartz. The points FGH show that, with increasing concentration of HF in the system, the percentage of dissolved volatile components increases, and the temperature of the liquidus field boundary decreases accordingly.

In Figure 32, the liquidus field boundary has been

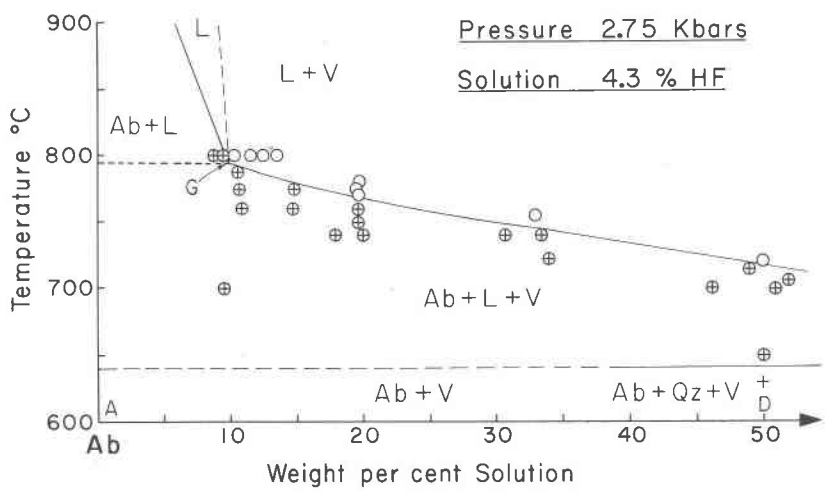

Fig. 29. Phase fields intersected by the join AD (Fig. 27) in the system Ab–H_2O–HF (Wyllie and Tuttle, 1959, unfinished manuscript).

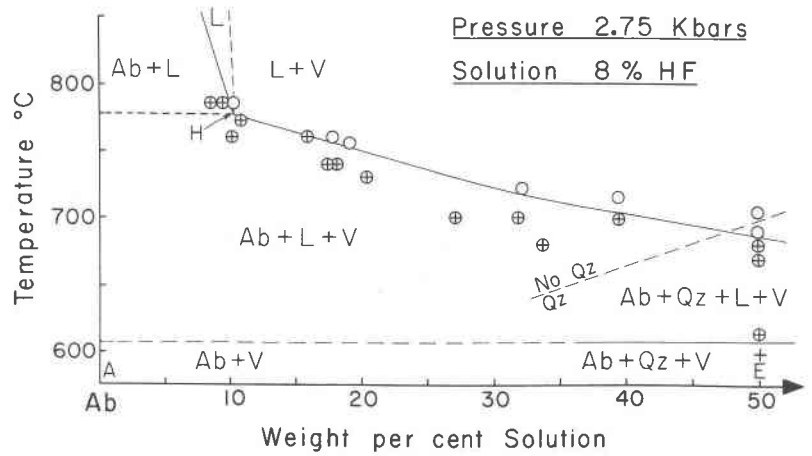

Fig. 30. Phase fields intersected by the join AE (Fig. 27) in the system Ab–H_2O–HF (Wyllie and Tuttle, 1959, unfinished manuscript).

passed through the determined points FGH in the composition triangle, and the dashed line represents the corresponding vaporus field boundary, V(Ab,L). The field boundary is barely visible in terms of weight percent, so it has been replotted in molecular percent in Figure 32B.

Figure 33A is a schematic isobaric isothermal section with a three-phase triangle intersected by two composition joins, AS_1 and AS_2. Experimental location of points such as M and N between the three-phase and two-phase fields gives the orientation of isothermal liquid–vapor phase boundaries, which are graphical representations of the distribution of H_2O and HF between liquid and vapor. From the results in Figures 29 and 30, at temperatures where the phase relationships intersected appear to remain ternary, isothermal lines corresponding to MNP have been constructed for four temperatures in Figure 33B. The results recalculated in molecular percent in Figure 33C show that through the temperature interval from 808° to 700°C the vapor remains very rich in H_2O, with HF preferentially dissolved in the liquid.

Some other fugitive components

The results for HF in Figures 29–33 indicate that for moderate concentrations of HF its main effect is that of a flux. This contrasts with results obtained for HCl, which is strongly reactive. The main effect of

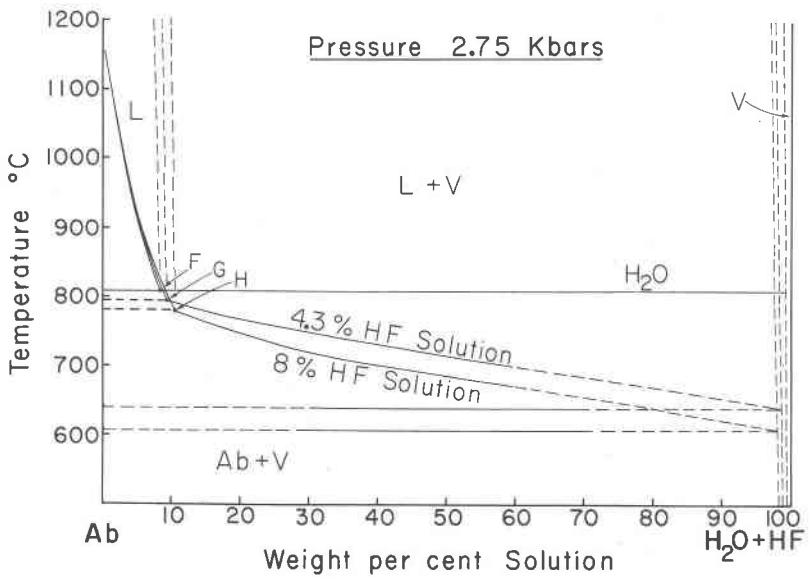

Fig. 31. The system Ab–H_2O–HF; superimposed phase diagrams from Figs. 28, 29, 30 (Wyllie and Tuttle, 1959, unfinished manuscript).

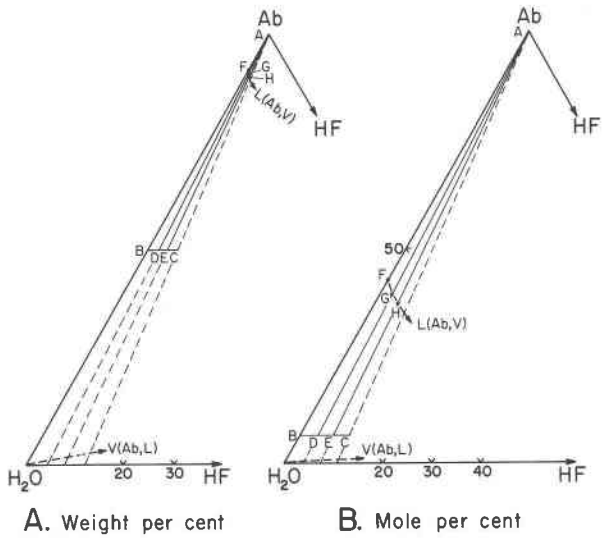

Fig. 32. System Ab–H_2O–HF at 2.75 kbar. Points F, G. H on the vapor-saturated liquidus field boundary, as determined in Figs. 28, 29, and 30 (Wyllie and Tuttle, 1959, unfinished manuscript).

HCl is to destroy the albite (or feldspar in granite) and to transfer the alkalis, particularly sodium, into the vapor phase (Wyllie and Tuttle, 1964).

In an attempt to reduce the destructive reaction and compare the behavior of F and Cl, Koster van Groos and Wyllie (1968, 1969) studied the phase relationships in the systems Ab–NaF–H_2O and Ab–NaCl–H_2O. The results confirmed the conclusions reached from the studies made using HF and HCl: namely, fluorine tends to remain in the silicate liquid, whereas chlorine is enriched in the vapor phase compared with liquid, through most of the system.

Another result from these silicate–salt–H_2O systems demonstrates that even a trace of "mineralizers" such as NaF could cause a significant increase in the H_2O content of residual melts, compared with values for silicate–H_2O systems (Fig. 18). For example, at 1 kbar, the melting of albite with H_2O at 910°C produces a liquid with 4.2 percent H_2O. With addition of NaF the temperature of beginning of melting is lowered to 688°C, and the liquid contains 30 weight percent H_2O. The effect of NaCl is less marked, but addition of NaCl to the system Ab–H_2O approximately doubles the solubility of H_2O at 1 kbar.

The effect of CO_2 in addition to H_2O was explored using H_2O–CO_2 mixtures with albite and granite (Wyllie and Tuttle, 1959), and then by adding CO_2 to silicate–H_2O systems in the form of Na_2CO_3 or

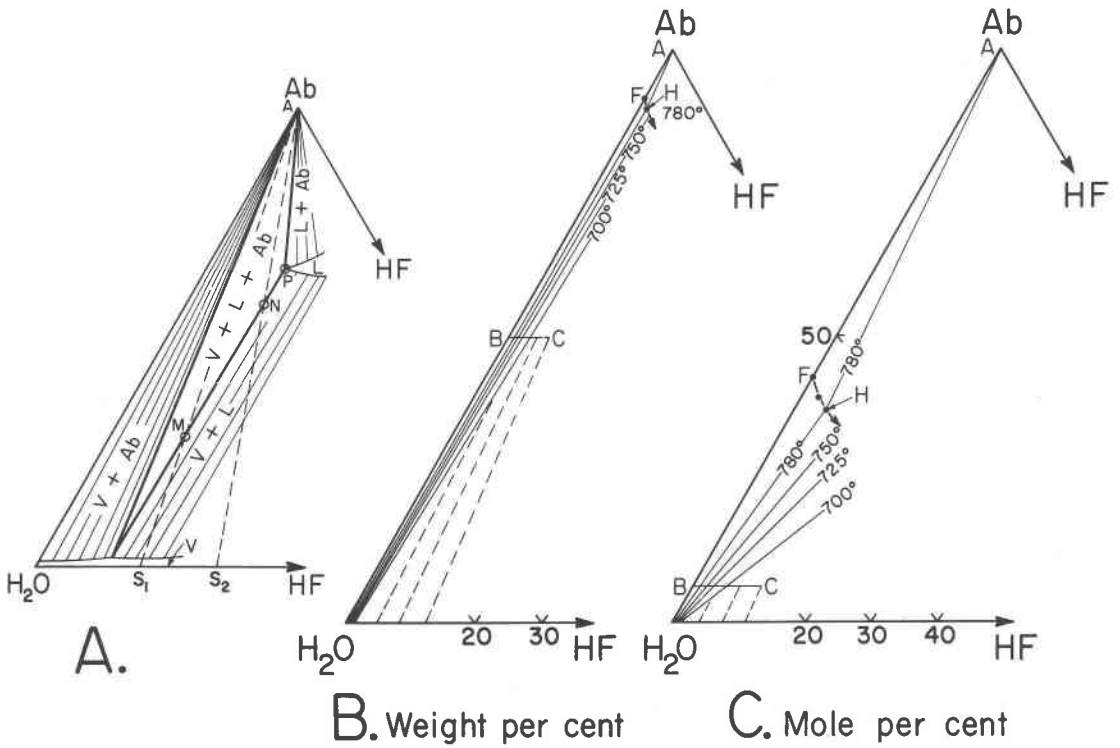

Fig. 33. System Ab–H_2O–HF at 2.75 kbar. (A) Schematic representation of isobaric isothermal section, showing the intersections of two composition joins, AS_1 and AS_2 with the side PMN of a three-phase triangle. (B) and (C) Geometrical positions of L + V tie-lines determined from Figs. 29 and 30, showing the strong partition of HF from vapor into liquid (Wyllie and Tuttle, 1959, unfinished manuscript).

$CaCO_3$ (Koster van Groos and Wyllie, 1966, 1973; Watkinson and Wyllie, 1971). These experiments demonstrated the low solubility of CO_2 in granitic melts at low pressures, the existence of liquid immiscibility between some silicate and carbonate liquids, and the existence for other compositions of paths of crystallization that lead to liquids greatly enriched in carbonate components.

These few results suffice to confirm that the volatile components dissolved in magmas can produce a wide range of effects during the closing stages of crystallization. It is in residual magmas that they are most influential.

Residual magmas

Experimental studies on silicate–volatile component systems have provided much information about the origin and crystallization of pegmatites and carbonatites, although details about the effects of many of the fugitive constituents that escaped from the natural systems have not been determined.

Pegmatites are associated with granitic plutons, and they represent residual granitic melts enriched in dissolved H_2O. A comprehensive model for the derivation and crystallization of pegmatites was presented by Jahns and Burnham (1969), using the kind of experimental data summarized in Figure 26. A granite magma originally undersaturated with H_2O cools and crystallizes, and during the late stages of crystallization a separate aqueous vapor phase is exsolved. This stage is associated with the growth of large crystals and other textural features recorded in pegmatites.

Carbonatite intrusions are associated with plutonic complexes dominated by nepheline syenites and other subsilicic alkalic rocks. They are characterized by distinctive assemblages of minor and trace elements, as well as an extraordinary concentration of CO_2. These probably represent residual magmas derived either through extensive fractional crystallization of a parent subsilicic alkalic magma which was derived ultimately from mantle peridotite enriched in CO_2 and other volatile components (at some temperature above the solidus surface WZmnQN in Fig. 8), or by the separation from a similar parent magma of an immiscible carbonatite magma (Heinrich, 1966). Small bodies of carbonatite are associated with some kimberlites. These bodies may be related more directly to CO_2 from the mantle, dissolved in the kimberlitic magma derived by partial melting of mantle enriched in volatile components, somewhere in the region above the line QdN in Figure 8.

The crystallization of carbonatites has been modelled experimentally in several silicate–carbonate–H_2O–CO_2 systems, and the final liquid precipitating calcite and other minerals normally terminates at a eutectic precipitating portlandite (*e.g.* Wyllie, 1966). The absence of portlandite in carbonatites has found no satisfactory explanation in synthetic systems until recently. I am pleased to report that in the system CaO–MgO–CO_2–H_2O at 2 kbar M. F. Fanelli has discovered a second low-temperature eutectic, separated from the portlandite–calcite eutectic by a thermal maximum on the liquidus surface, approximately along the join $CaCO_3$–$Mg(OH)_2$. At this eutectic, calcite, dolomite and periclase are precipitated with evolution of H_2O-rich vapor. Addition of SiO_2 to the system would provide a eutectic liquid precipitating calcite, dolomite, and magnesian silicates at temperatures below 650°C, with no portlandite (Fanelli and Wyllie, manuscript in preparation).

Concluding remarks

Important but inadequately understood factors include the sources of the volatile components, in deep undetermined reservoirs or recycled to uncertain depths through subduction, and the variation of temperature and oxygen fugacity with depth in various tectonic environments. The experimental data available at present show that the subsilicic, alkalic magmas related to kimberlite in composition can be generated from mantle peridotite containing CO_2 in the form of dolomite. In fact, it is difficult to see how they could be generated without the involvement of dolomite. But it is not certain that the oxygen fugacity at 100 km depth is high enough to oxidize carbon to carbonate. Perchuk (1977) concluded that mantle fluids are reduced gases perhaps derived by the decomposition of oxides, hydrides, carbides, sulfides, nitrides, and halogens of alkali metals at great depths. According to his review and calculations, it is only within the crust, in the pressure range 8 to 3 kbar, that reduced pore fluids are sharply enriched in H_2O and CO_2 by oxidation. It would be desirable to investigate the effect of reduced gases on the compositions of liquids derived from peridotite at high pressures.

Progress in understanding the behavior of volatile components in magmas depends upon the determination of phase diagrams for rocks and synthetic systems, including solubility measurements and thermodynamic properties. The role of H_2O and CO_2 in silicate melts with respect to their solubilities and the degree of polymerization of liquid structure has been

reviewed by Burnham (1975) and Mysen (1976, 1977). Additional studies are needed on SO_2.

I would like to end with a final note of caution. The results for the system $NaAlSi_3O_8$–H_2O–HF are real data, and the results for basalt–andesite–rhyolite–H_2O are based on real data, but many large gaps have been crudely patched over. The phase diagrams for the system peridotite–CO_2–H_2O, however, represent an incomplete synthesis of sketchy phase equilibrium results from scattered sources. The use of deduced phase diagrams, according to Bowen (1928, preface) "feels out the strengths and weaknesses of our adversaries, the rocks, and thus lays a necessary foundation for a more serious campaign of experimental attack, concentrated upon these points where progress is most likely to be made." I present these partly schematic phase diagrams in the same spirit.

Acknowledgments

This research was supported by NSF grants EAR 76-20410 and EAR 76-20413 (Earth Sciences Section). I thank also the many graduate students and research associates who have helped gather the data that guided my pencil in the construction of the phase diagrams, and A. L. Boettcher for review of some of the figures.

References

Allen, J. C. and A. L. Boettcher (1978) Amphiboles in andesite and basalt: II. Stability as a function of P–T–f_{H_2O}–f_{O_2}. *Am. Mineral., 63,* 1074–1087.

———, ——— and G. Marland (1975) Amphiboles in andesite and basalt: I. Stability as a function of P–T–f_{O_2}. *Am. Mineral., 60,* 1069–1085.

Anderson, A. T. (1975) Some basaltic and andesitic gases. *Rev. Geophys. Space Phys. 13,* 37–55.

Anderson, R. N., S. Uyeda and A. Miyashiro (1976) Geophysical and geochemical constraints at converging plate boundaries—Part I: Dehydration in the downgoing slab. *Geophys. J. R. Astron. Soc., 44,* 333–357.

———, S. E. DeLong and W. M. Schwarz (1978) Thermal model for subduction with dehydration in the downgoing slab. *J. Geol., 86,* 731–739.

Andrews, D. J. and N. H. Sleep (1974) Numerical modelling of tectonic flow behind island arcs. *Geophys. J. R. Astron. Soc., 38,* 237–251.

Bowen, N. L. (1928) *The Evolution of the Igneous Rocks.* Princeton University Press, Princeton.

Brown, G. M. and J. F. Schairer (1971) Chemical and melting relations of some calc-alkaline volcanic rocks. *Geol. Soc. Am. Mem., 30,* 139–157.

———, J. G. Holland, H. Sigurdsson, J. F. Tomblin and R. J. Arculus (1977) Geochemistry of the Lesser Antilles volcanic island arc. *Geochim. Cosmochim. Acta, 41,* 785–801.

Burnham, C. W. (1975) Water and magmas: a mixing model. *Geochim. Cosmochim. Acta, 39,* 1077–1084.

——— and R. H. Jahns (1962) A method of determining the solubility of water in silicate melts. *Am. J. Sci., 260,* 721–745.

Chen, C.-H. and D. C. Presnall (1975) The system Mg_2SiO_4–SiO_2 at pressures up to 25 kilobars. *Am. Mineral., 60,* 398–406.

Clark, S. P. and A. E. Ringwood (1964) Density distribution and constitution of the mantle. *Rev. Geophys., 2,* 35–88.

Delaney, J. R., D. W. Muenow and D. G. Graham (1978) Abundance and distribution of water, carbon and sulfur in the glassy rims of submarine pillow basalts. *Geochim. Cosmochim. Acta, 42,* 581–594.

Delany, J. M. and H. C. Helgeson (1978) Calculation of the thermodynamic consequences of dehydration in subducting oceanic crust to 100 kb and >800°C. *Am. J. Sci., 278,* 638–686.

Eggler, D. H. (1972) Water-saturated and undersaturated melting relations in a Paricutin andesite and an estimate of water content in the natural magma. *Contrib. Mineral. Petrol., 34,* 261–271.

——— (1973) Principles of melting of hydrous phases in silicate melt. *Carnegie Inst. Wash. Year Book, 72,* 491–495.

——— (1974) Effect of CO_2 on the melting of peridotite. *Carnegie Inst. Wash. Year Book, 73,* 215–224.

——— (1975) CO_2 as a volatile component of the mantle: the system Mg_2SiO_4–SiO_2–H_2O–CO_2. *Phys. Chem. Earth, 9,* 869–881.

——— (1976) Does CO_2 cause partial melting in the low-velocity layer of the mantle? *Geology, 4,* 69–72.

——— (1977) The principle of the zone of invariant vapor composition: an example in the system CaO–MgO–SiO_2–CO_2–H_2O and implications for the mantle solidus. *Carnegie Inst. Wash. Year Book, 76,* 428–435.

——— (1978) The effect of CO_2 upon partial melting of peridotite in the system Na_2O–CaO–Al_2O_3–MgO–SiO_2–CO_2 to 35 kb, with an analysis of melting in a peridotite–H_2O–CO_2 system. *Am. J. Sci., 278,* 305–343.

Ellis, D. and P. J. Wyllie (1979a) Carbonation, hydration, and melting relations in the system MgO–H_2O–CO_2 at pressures up to 100 kbar. *Am. Mineral., 64,* 32–40.

——— and ——— (1979b) Hydration and melting reactions in the system MgO–SiO_2–H_2O at pressures up to 100 kbar. *Am. Mineral., 64,* 41–48.

——— and ——— (1979c) A model of phase relations in the system MgO–SiO_2–H_2O–CO_2 and prediction of the compositions of liquids coexisting with forsterite and enstatite. *Proc. 2nd Int. Kimberlite Conf.,* in press.

Fyfe, W. S. and A. R. McBirney (1975) Subduction and the structure of andesitic volcanic belts. *Am. J. Sci., 275-A,* 285–297.

Green, D. H. (1973a) Experimental melting studies on a model upper mantle composition at high pressure under water-saturated and water-undersaturated conditions. *Earth Planet. Sci. Lett., 19,* 37–53.

——— (1973b) Contrasted melting relations in a pyrolite upper mantle under mid-oceanic ridge, stable crust and island arc environments. *Tectonophysics, 17,* 285–297.

——— (1976) Experimental testing of "equilibrium" partial melting of peridotite under water-saturated, high-pressure conditions. *Can. Mineral., 14,* 255–268.

——— and R. C. Liebermann (1976) Phase equilibria and elastic properties of a pyrolite model for the oceanic upper mantle. *Tectonophysics, 32,* 61–92.

Green, T. H. (1972) Crystallization of calc-alkaline andesite under controlled high-pressure hydrous conditions. *Contrib. Mineral. Petrol., 34,* 150–166.

——— and A. E. Ringwood (1968) Genesis of the calc-alkaline igneous rock suite. *Contrib. Mineral. Petrol., 18,* 105–162.

——— and ——— (1972) Crystallization of garnet-bearing rhyodacite under high-pressure hydrous conditions. *J. Geol. Soc. Aust., 19,* 203–212.

Hasebe, R., N. Fujii and S. Uyeda (1970) Thermal processes under island arcs. *Tectonophysics, 10,* 335–355.

Heinrich, E. W. (1966) *The Geology of Carbonatites.* Rand McNally and Co., Chicago.

Holloway, J. R. (1976) Fluids in the evolution of granitic magmas: consequences of finite CO_2 solubility. *Bull. Geol. Soc. Am., 87,* 1513–1518.

——— and D. H. Eggler (1976) Fluid-absent melting of peridotite containing phlogopite and dolomite. *Carnegie Inst. Wash. Year Book, 75,* 636–639.

Huang, W. L. and P. J. Wyllie (1973) Melting relations of muscovite-granite to 35 kbar as a model for fusion of metamorphosed subducted oceanic sediments. *Contrib. Mineral. Petrol., 42,* 1–14.

Jahns, R. H. and C. W. Burnham (1969) Experimental studies of pegmatite genesis: I. A model for the derivation and crystallization of granitic pegmatites. *Econ. Geol., 64,* 843–864.

Jordan, T. H. (1975) The continental lithosphere. *Rev. Geophys. Space Phys., 13,* 1–12.

Kitahara, S., S. Takenouchi and G. C Kennedy (1966) Phase relations in the system $MgO–SiO_2–H_2O$ at high temperatures and pressures. *Am. J. Sci., 264,* 223–233.

Koster van Groos, A. F. and P. J. Wyllie (1966) Liquid immiscibility in the system $Na_2O–Al_2O_3–SiO_2–CO_2$ at pressures up to 1 kilobar. *Am. J. Sci., 264,* 234–255.

——— and ——— (1968) Melting relationships in the system $NaAlSi_3O_8–NaF–H_2O$ to 4 kilobars pressure. *J. Geol., 76,* 50–70.

——— and ——— (1969) Melting relationships in the system $NaAlSi_3O_8–NaCl–H_2O$ at 1 kilobar pressure, with petrological applications. *J. Geol., 77,* 581–605.

——— and ——— (1973) Liquid immiscibility in the join $NaAlSi_3O_8–CaAlSi_2O_8–Na_2CO_3–H_2O$. *Am. J. Sci., 273,* 465–487.

Kushiro, I. (1972) Effect of water on the composition of magmas formed at high pressures. *J. Petrol., 13,* 311–334.

Lambert, I. B. and P. J. Wyllie (1968) Stability of hornblende and a model for the low velocity zone. *Nature, 219,* 1240–1241.

——— and ——— (1972) Melting of gabbro (quartz eclogite) with excess water to 35 kilobars, with geological applications. *J. Geol., 80,* 693–708.

Marsh, B. D. (1978) On the cooling of ascending andesitic magma. *Phil. Trans. R. Soc. Lond., A288,* 611–625.

McGetchin, T. R. and J. R. Besancon (1973) Carbonate inclusions in mantle-derived pyrope. *Earth Planet. Sci. Lett., 18,* 408–410.

Millhollen, G. L., A. J. Irving and P. J. Wyllie (1974) Melting interval of peridotite with 5.7 per cent water to 30 kilobars. *J. Geol., 82,* 575–587.

Miyashiro, A. (1975) Island arc volcanic rock series: a critical review. *Petrologie, 1,* 177–187.

Moore, J. G. (1965) Petrology of deep-sea basalt near Hawaii. *Am. J. Sci., 263,* 40–52.

———, J. N. Batchelder and C. G. Cunningham (1977) CO_2–filled vesicles in mid-ocean basalt. *J. Volcanol. Geothermal Res., 2,* 309–327.

Mysen, B. O. (1976) The role of volatiles in silicate melts: Solubility of carbon dioxide and water in feldspar, pyroxene, and feldspathoid melts to 30 kb and 1625°C. *Am. J. Sci., 276,* 969–996.

——— (1977) The solubility of H_2O and CO_2 under predicted magma genesis conditions and some petrological and geophysical implications. *Rev. Geophys. Space Phys., 15,* 351–361.

——— and A. L. Boettcher (1975) Melting of a hydrous mantle. *J. Petrol., 16,* 520–548, 549–593.

——— and I. Kushiro (1977) Compositional variations of coexisting phases with degree of melting of peridotite in the upper mantle. *Am. Mineral., 62,* 843–856.

Nehru, C. E. and P. J. Wyllie (1975) Compositions of glasses from St. Paul's peridotite partially melted at 20 kilobars. *J. Geol., 83,* 455–471.

Nicholls, I. A. (1974) Liquids in equilibrium with peridotitic mineral assemblages at high water pressures. *Contrib. Mineral. Petrol., 45,* 289–316.

——— and A. E. Ringwood (1973) Effect of water on olivine stability in tholeiites and the production of silica-saturated magmas in the island-arc environment. *J. Geol., 81,* 285–300.

Oxburgh, E. R. and D. L. Turcotte (1970) Thermal structure of island arcs. *Geol. Soc. Am. Bull., 81,* 1665–1688.

Perchuk, L. L. (1977) Thermodynamic control of metamorphic processes. In S. K. Saxena and S. Bhattacharji, Eds., *Energetics of Geological Processes,* p. 285–352. Springer-Verlag, New York.

Piwinskii, A. J. (1973) Experimental studies of igneous rock series, central Sierra Nevada batholith, California: Part II. *Neues Jahrb. Mineral. Monatsh.,* 193–215.

Presnall, D. C. (1979) A double seismic low-velocity zone in the mantle beneath mid-ocean ridges. *Earth Planet. Sci. Lett.,* in press.

Ringwood, A. E. (1975) *Composition and Petrology of the Earth's Mantle.* McGraw-Hill, New York.

Rosenhauer, M., E. Woermann, B. Knecht and G. C. Ulmer (1977) The stability of graphite and diamond as a function of the oxygen fugacity in the mantle. *Second Int. Kimberlite Conf. Extended Abstracts,* Santa Fe, October 1977.

Scarfe, C. M. and P. J. Wyllie (1967) Serpentine dehydration curves and their bearing on serpentinite deformation in orogenesis. *Nature, 215,* 945–946.

Solomon, S. C. (1976) Geophysical constraints on radial and lateral temperature variations in the upper mantle. *Am. Mineral., 61,* 788–803.

Stern, C. R. (1974) Melting products of olivine tholeiite basalt in subduction zones. *Geol., 2,* 227–230.

———, W. L. Huang and P. J. Wyllie (1975) Basalt–andesite–rhyolite–H_2O: crystallization intervals with excess H_2O and H_2O-undersaturated liquidus surfaces to 35 kilobars with implications for magma genesis. *Earth Planet. Sci. Lett., 28,* 189–196.

——— and P. J. Wyllie (1973a) Water-saturated and undersaturated melting relations of granite to 35 kilobars. *Earth Planet. Sci. Lett., 18,* 163–167.

——— and ——— (1973b) Melting relations of basalt–andesite–rhyolite–H_2O and a pelagic red clay at 30 kbars. *Contrib. Mineral. Petrol., 42,* 313–323.

——— and ——— (1978) Phase compositions through crystallization intervals in basalt–andesite–H_2O at 30 kbar, with implications for subduction zone magmas. *Am. Mineral., 63,* 641–663.

Toksöz, M. N., J. W. Minear and B. R. Julian (1971) Temperature field and geophysical effects of a downgoing slab. *J. Geophys. Res., 76,* 1113–1138.

Walker, D., E. M. Stolper and J. F. Hays (1978) A numerical treatment of melt/solid segregation: size of the eucrite parent body and stability of the terrestrial low-velocity zone. *J. Geophys. Res., 83,* 6005–6013.

Watkinson, D. H. and P. J. Wyllie (1971) Experimental study of the join $NaAlSiO_4–CaCO_3–H_2O$ and the genesis of alkalic rock–carbonatite complexes. *J. Petrol., 12,* 357–378.

Woermann, E., B. Knecht, M. Rosenhauer and G. C. Ulmer (1977) The stability of graphite in the system C–O. *Second Int. Kimberlite Conf., Extended Abstracts,* Santa Fe, October 1977.

Wyllie, P. J. (1966) Experimental studies of carbonatite problems: the origin and differentiation of carbonatite magmas. In O. F. Tuttle and J. Gittins, Eds., *The Carbonatites,* p. 311–352. Wiley, New York.

——— (1971) *The Dynamic Earth: a Textbook in Geosciences.* Wiley, New York.

——— (1973) Experimental petrology and global tectonics: a preview. *Tectonophysics, 17,* 189–209.

——— (1974) Limestone assimilation. In H. Sørensen, Ed., *Alkaline Rocks,* Chapter VI.3, p. 459–474. Wiley, New York.

——— (1977a) Mantle fluid compositions buffered by carbonates in peridotite–CO_2–H_2O. *J. Geol., 85,* 187–207.

——— (1977b) Crustal anatexis: an experimental review. *Tectonophysics, 43,* 41–71.

——— (1977c) From crucible through subduction to batholiths. In S. K. Saxena and S. Bhattacharji, Eds., *Energetics of Geological Processes,* p. 389–433. Springer-Verlag, New York.

——— (1978) Mantle fluid compositions buffered in peridotite–CO_2–H_2O by carbonates, amphibole, and phlogopite. *J. Geol., 86,* 687–713.

——— (1979) Water and magma generation at subduction zones. *Bull. Volcanol.,* in press.

——— and W. L. Huang (1975) Peridotite, kimberlite, and carbonatite explained in the system CaO–MgO–SiO_2–CO_2. *Geology, 3,* 621–624.

——— and ——— (1976) Carbonation and melting reactions in the system CaO–MgO–SiO_2–CO_2 at mantle pressures with geophysical and petrological applications. *Contrib. Mineral. Petrol., 54,* 79–107.

——— and O. F. Tuttle (1959) Effect of carbon dioxide on the melting of granite and feldspars. *Am. J. Sci., 257,* 648–655.

——— and ——— (1960) Experimental investigation of silicate systems containing two volatile components, Part 1. Geometrical considerations. *Am. J. Sci., 258,* 498–517.

——— and ——— (1961) Experimental investigation of silicate systems containing two volatile components, Part II. The effects of NH_3 and HF, in addition to H_2O, on the melting temperatures of albite and granite. *Am. J. Sci., 259,* 128–143.

——— and ——— (1964) Experimental investigation of silicate systems containing two volatile components. Part III. The effects of SO_3, P_2O_5, HCl, and Li_2O, in addition to H_2O, on the melting temperatures of albite and granite. *Am. J. Sci., 262,* 930–939.

Yamamoto, K. and S. Akimoto (1977) The system MgO–SiO_2–H_2O at high pressures and temperatures—stability field for hydroxyl-chondrodite, hydroxyl-clinohumite and 10 A-phase. *Am. J. Sci., 277,* 288–312.

Yoder, H. S. (1976) *Generation of Basaltic Magma.* Nat. Acad. Sci., Washington, DC.

Manuscript received, January 22, 1979.
accepted for publication, January 22, 1979.